Computational Fluid Dynamics Modeling and Experimental Investigation of a Chemical Vapor Deposition Synthesis of ZnO Nanostructures

by

Timothy J. Daugherty

Submitted in Partial Fulfillment of the Requirements

for the Degree of

Master of Science

in the

Mechanical Engineering

Program

YOUNGSTOWN STATE UNIVERSITY

May, 2016

Computational Fluid Dynamics Modeling and Experimental Investigation of a Chemical Vapor Deposition Synthesis of ZnO Nanostructures

Timothy J. Daugherty

I hereby release this thesis to the public. I understand that this thesis will be made available from the OhioLINK ETD Center and the Maag Library Circulation Desk for public access. I also authorize the University or other individuals to make copies of this thesis as needed for scholarly research.

Signature:

Timothy J. Daugherty, Student Date

Approvals:

Dr. C. Virgil Solomon, Thesis Advisor Date

Dr. Stefan Moldovan, Committee Member Date

Dr. Kyosung Choo, Committee Member Date

Dr. Salvatore A. Sanders, Dean of Graduate Studies Date

Abstract

Zinc oxide (ZnO) thin films and nanostructures have received extensive attention as important materials for various applications in field-effect transistors, gas sensors, dye-sensitized solar cell, and ultraviolet photodetectors. Thermal transport methods are some of the most common synthesis methods, due perhaps to the relative simplicity of the experimental setup which involves a temperature-controlled tube furnace and pure Zn as starting material. Thin films and nanostructures with various morphologies and sizes can be obtained using this method and varying experimental parameters such as synthesis temperature, air or oxygen flow rate, morphology of Zn sources, position of substrate, etc. So far, most researchers have used quasi-empirical methods to determine the optimum growth conditions for specific ZnO morphologies. The purpose of this research is to use computational fluid dynamics (CFD) to understand the influence of thermal evaporation parameters (furnace temperature, gas flow, substrate position) on the morphology and size of ZnO nanostructures. ZnO synthesis was performed under controlled conditions and the products were analyzed via scanning electron microscopy (SEM) analysis. The process was then simulated numerically using two- and three-dimensional models in ANSYS Fluent 16.1.0 software.

Acknowledgements

The use of the research facilities within the Department of Mechanical & Industrial Engineering and Center for Excellence in Advanced Materials Analysis, STEM College at Youngstown State University is gratefully acknowledged.

The author also gratefully acknowledges the use of YSU's Electron Microscopy Facility and the National Science Foundation support (DMR #1229129) for this work.
The assistance of Dr. Solomon and Dr. Moldovan is greatly appreciated, as this work would not exist without their support and encouragement.

Additionally, the author extends his sincerest thanks to Dr. Virgil Solomon and Dr. Stefan Moldovan, without whom this work would not have been possible. Additionally the author would like to thank Dr. Kyosung Choo for participating on the committee for this thesis.

Last, but certainly not least, the kind support of friends and family is gratefully acknowledged. Their encouragement is what made this work possible.

Table of Contents

List of Figures

Chapter 1: Introduction

Zinc oxide (ZnO) is a notable semiconductor for its physical properties as well as its ability to form a wide variety of unique nanostructures. Thin films and nanostructures of zinc oxide have received large amounts of attention as potential materials for use in field-effect transistors, gas sensors, and ultraviolet photodetectors [1-3]. As a semiconductor, zinc oxide has a direct-wide-band gap energy of 3.37eV and a large exciton binding energy of 60 meV at room temperature, which makes zinc oxide a good candidate for a large range of applications. Research into the synthesis and application of zinc oxide has been conducted since 1945 [4].

1.1 Synthesis Methods

A number of methods have been used to produce ZnO nanostructures. Among them are methods such as metal catalytic growth (commonly called vapor-liquid-solid or VLS), radio-frequency magneton sputtering, pulsed laser deposition (PLD), both organometallic and thermal chemical vapor deposition (MOCVD and CVD, respectively), thermal evaporation, and molecular beam epitaxy (MBE) [5-7]. Each process has advantages and disadvantages, and can lead to vastly different product morphology.

1.1.1 Vapor-Liquid-Solid

The metal catalytic growth method of synthesizing zinc oxide has been in use since 1964 [4]. The method uses a metal catalyst on the target substrate in order to nucleate and direct the growth of the product. Common catalysts include gold, copper, tin, and platinum. In the typical VLS synthesis process, the substrate will be sputter-coated or otherwise covered in a thin layer of catalyst. It will then be placed in a furnace, either on a stage or in a boat, which will be kept under controlled pressure conditions while an inert carrier gas is allowed to flow through the furnace. Zinc is also placed in the furnace, either as powdered zinc oxide, or as a zinc metal powder which is heated in the presence of oxygen gas. As the furnace is heated, the catalyst melts and absorbs zinc oxide vapor. The nanoscale drop of molten catalyst becomes supersaturated and zinc oxide begins to precipitate at the bottom of the drop. Over time, the catalyst will rise up as more and more layers are deposited, resulting in the eventual growth of a zinc oxide nanowire [8]. A diagram of this process can be seen below.

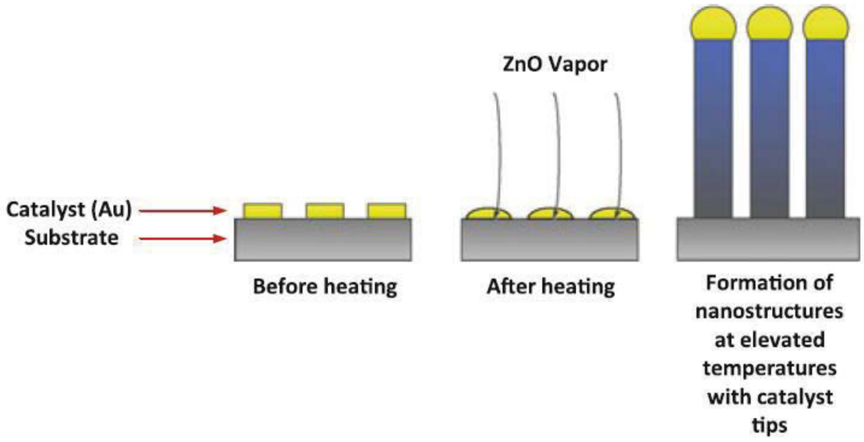

Figure 1 - Vapor-liquid-solid process diagram [4]

Example of the ZnO nanostructures produced by VLS can be seen in Figure 2. Both images in the figure are SEM micrographs of nanowires grown by the VLS method. The top half of Figure 2 is a top-down view of the substrate, with each region corresponding to different substrate preparation methods. Figure 2b is a detailed view of the nanostructures produced by this process.

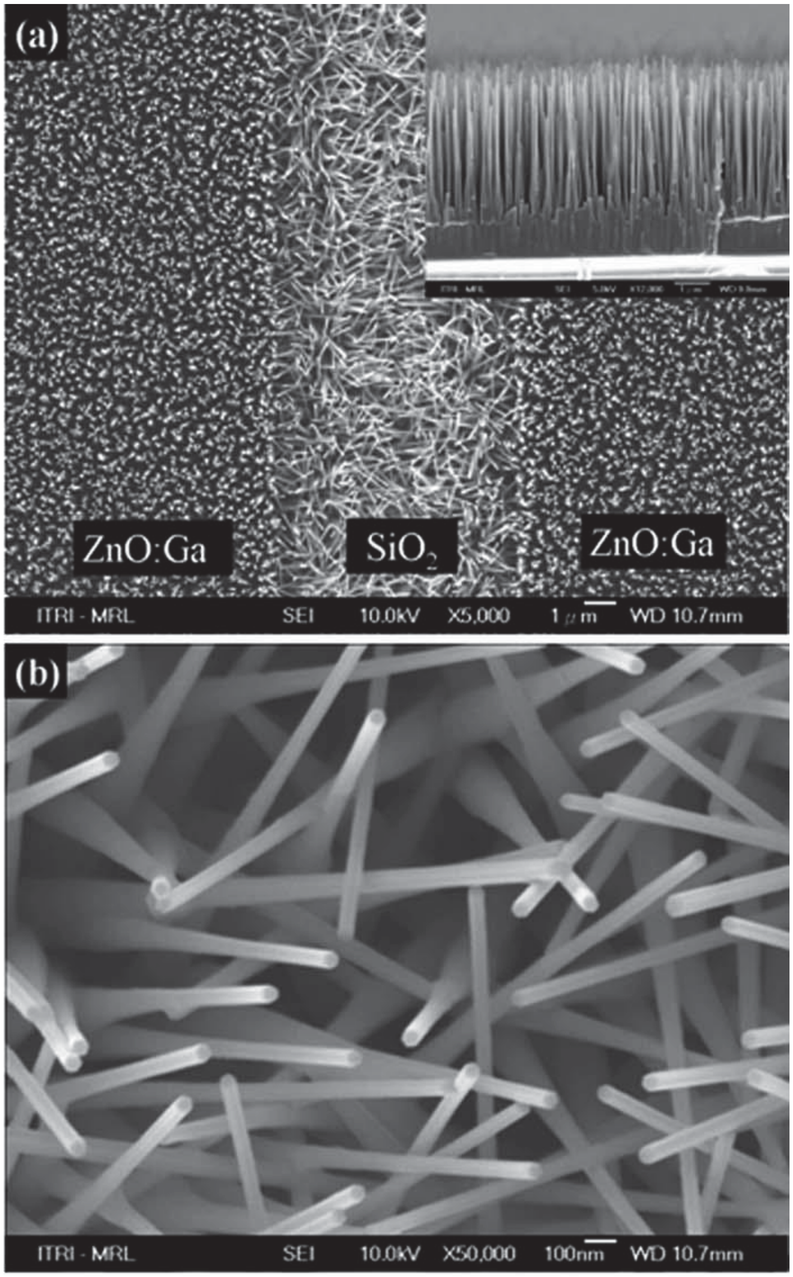

Figure 2 - ZnO nanowires grown by VLS [8].

The VLS method is attractive because the resulting morphology can be controlled by the size and shape of the catalyst. Additionally, the VLS method is easy to control and relatively easy to set up. Unfortunately, though, the metal catalyst will inevitably contaminate the resulting nanostructures, meaning that this method is undesirable in applications where high purity nanowires are desired.

1.1.2 Physical Vapor Deposition

Physical vapor deposition (PVD) is sometimes referred to as the vapor-solid (VS) method, as opposed to the VLS method. PVD is distinct from VLS in that no catalyst is required for the deposition to occur. Whereas VLS utilized a catalyst to capture zinc oxide vapor and guide the deposition process, PVD uses a bare substrate and zinc oxide deposits on its surface due to a reduction in temperature. PVD processes commonly involve an inert carrier gas flowing over a zinc oxide source which is heated to the point of sublimation. The carrier gas blows the vapor downstream to a cooler part of the furnace, where the vapor deposits on the substrate [4]. A rough schematic of the typical process can be seen in Figure 3.

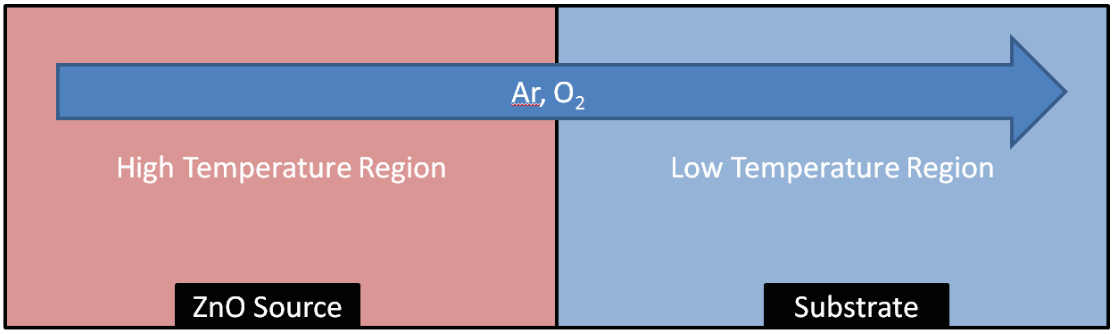

Figure 3 - Basic PVD experimental schematic

Several variations of PVD exist. Most variants of the process focus on heating the source material in different ways. Methods for vaporizing zinc oxide include the use of electron beams (electron beam physical vapor deposition, or EBPVD), cathode arcs (Arc-PVD), ion beam sputtering (IBS) and pulse laser deposition (PLD). These methods are designed to heat the source locally without needing to heat an entire furnace. Arc-PVD uses an electric arc, EBPVD uses a beam of electrons, and IBS uses a stream of ions to strike the source atoms hard enough that they are knocked into the air. PLD uses a pulsing laser to vaporize the source material so that it may float over the substrate and deposit.

PVD can synthesize nanowires either with a catalyst or without a catalyst, with gold being most commonly used [4]. The biggest advantage of PVD is the ability to synthesize nanostructures without a catalyst, which reduces the possibility of the metal catalyst contaminating the products of the reaction. According to Wang *et al*. [9], this process can produce ZnO nanowires under relatively low temperature conditions, but the products are very sensitive to experimental parameters, meaning that if this process were to be carefully controlled, it could be a method for producing inexpensive nanowires.

1.1.3 **Chemical Vapor Deposition**

Chemical vapor deposition (CVD) is performed in medium or low vacuum. Chemical precursors are allowed to flow over a substrate and react chemically to yield the desired products in a thin film on the substrate [10]. Compared to PVD, CVD is typically carried out at higher temperatures, and can often produce caustic or corrosive by-products [4]. A diagram of the basic CVD process can be seen in Figure 4.

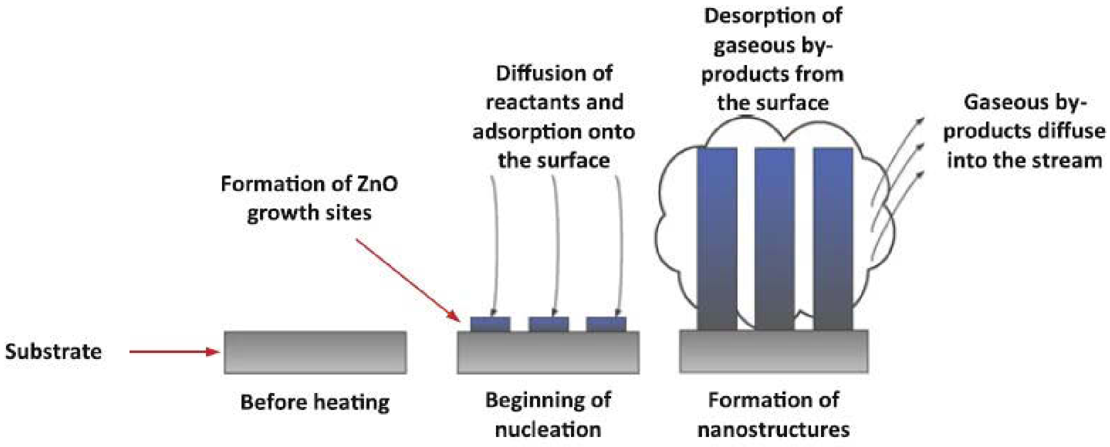

Figure 4 - CVD process diagram [4]

The CVD method covers three main approaches: atmospheric pressure (APCVD), low pressure (LPCVD) and plasma enhanced (PECVD) [4]. Each particular method has its own advantages and disadvantages. APCVD provides a high deposition rate and is easy to conduct because it can be conducted in atmospheric conditions, but it results in poor uniformity and the process prone to yielding contaminated products. LPCVD must be run under vacuum, has a lower deposition rate, and is conducted at higher temperatures, but produces a more evenly distributed product with fewer impurities. PECVD is a unique process in that it does not use a furnace to heat the zinc source. PECVD instead uses an electromagnetic field to excite the source under a vacuum, which causes the zinc to vaporize so that it may deposit on the target substrate [4].

CVD can result in a wide variety of nanostructures, including ‘nanonails’ (Figure 5), small semi-spherical particles (Figure 6), and hollow ‘urchins’ (Figure 7).

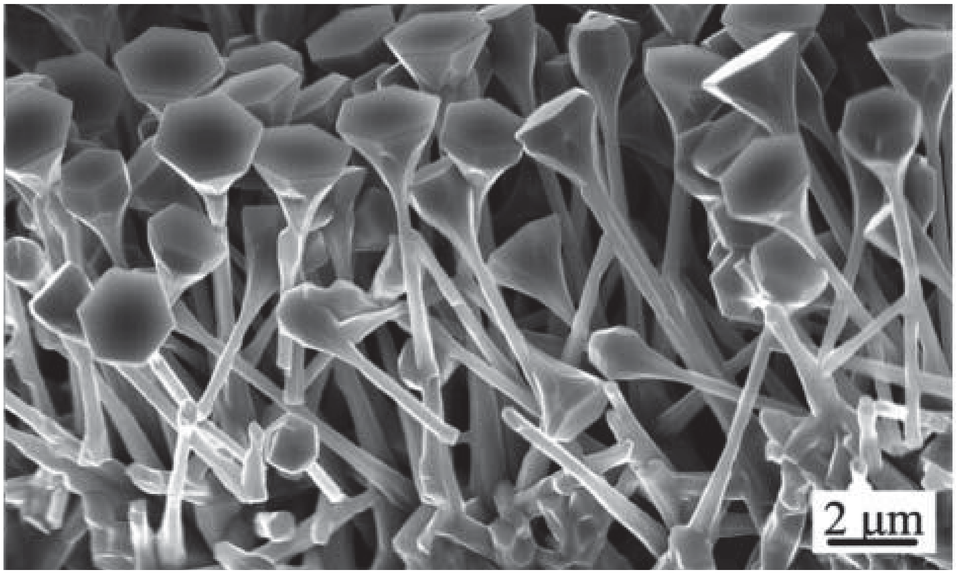

Figure 5 - ZnO nanonails [11]

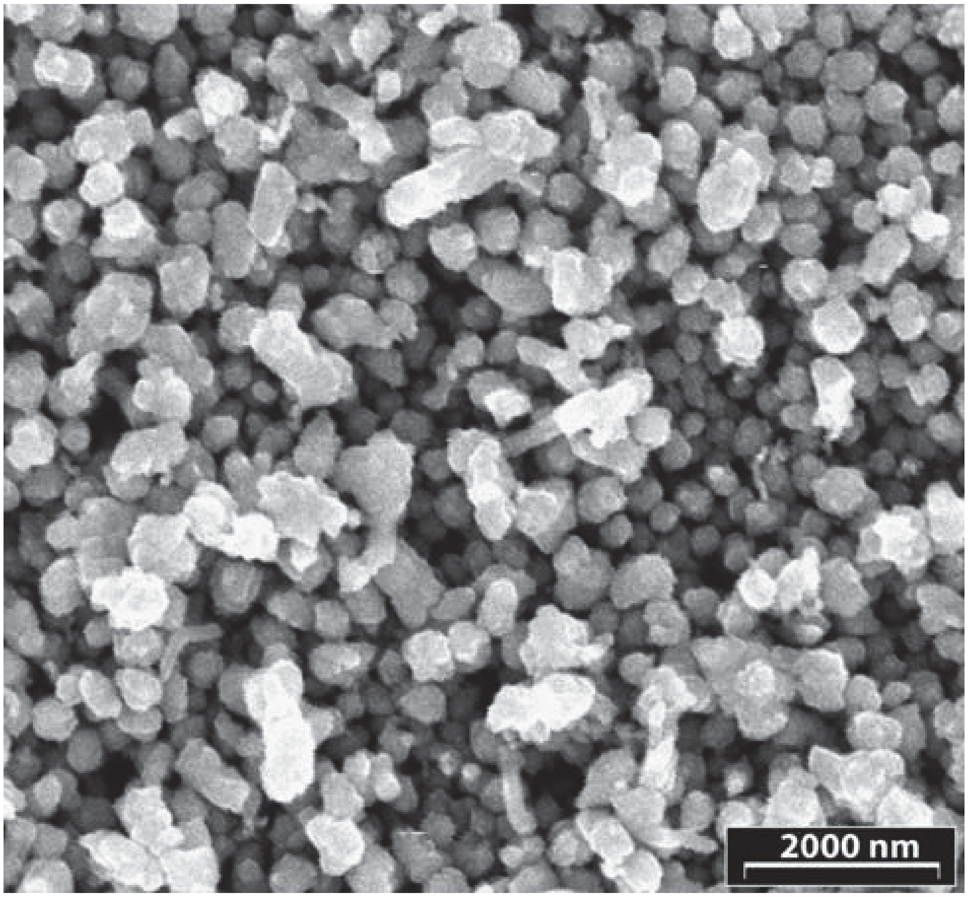

Figure 6 - Semi-spherical ZnO [12]

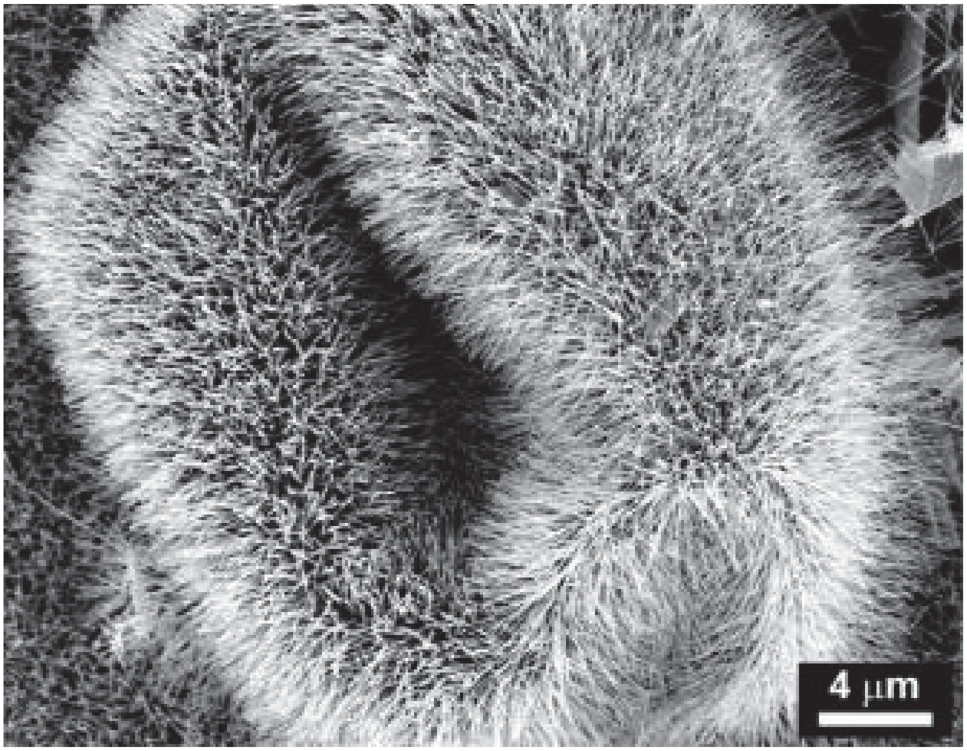

Figure 7 - Hollow ZnO 'urchin' [13]

1.2 Simulation of CVD Processes

1.2.1 Variation of Product Morphology

CVD is often used due to the low costs involved with experimental setup and process control. All that is needed to perform CVD to produce ZnO nanostructures is a temperature-controlled tube furnace, a substrate, and a zinc source. The process does not need a high vacuum and can yield a large variety of nanostructures which vary based on experimental parameters such as heating and cooling conditions, gas flow velocity, substrate and zinc position, and any other obstacles or geometry placed in the furnace to alter the flow of gasses.

The morphology and size of ZnO nanostructure product can also vary within a single process, with a single experiment producing multiple different structures. Kang, *et al*. determined that the position of the substrate in a reaction relative to the zinc source had a large effect on the final product structure [14]. For many practical applications, though, a specific structure is desired when synthesis of ZnO is performed. Optimizing the synthesis process to yield the maximum amount of desired product would be an important step in using specific zinc oxide nanostructures in a commercial setting. According to Tian *et al*. [15]a number of researchers have attempted to explain the various product morphologies in terms of experimental parameters, but these explanations were suppository and not backed by any evidence. Tian hypothesized that by computing properties such as the variation of gas concentration and temperature along the substrate, that correlations could be drawn between experimental parameters and observed product morphology.

1.2.2 Computational Fluid Dynamics

In order to determine properties such as gas velocity and pressure at multiple points in a CVD reactor without the need for excessive and obstructive instrumentation, fluid dynamics can be used to compute flow behavior. In trivial cases, this process involves solving basic partial differential equations with simple boundary conditions. In most non-trivial cases, assumptions must be made in order to make the equations solvable. In very complex equations, the equations simply cannot be solved analytically. In those cases, the equations must be solved numerically using a method known as computational fluid dynamics, or CFD.

At its core, CFD involves approximating partial differential equations as simple linear relations. The domain of interest is divides into a finite grid, commonly referred to as a mesh. As the mesh becomes finer, its elements become smaller and closer together, and the approximation will converge to the actual solution. Such a method is computationally intense, and therefore is best suited to be conducted using software. A number of CFD software packages and meshing utilities exist and are available for purchase.

Research has been done using CFD to analyze CVD synthesis of zinc oxide. Tian *et al*. [15] performed a simple CVD process by flowing oxygen and nitrogen through a tube furnace which contained pure zinc metal powder and a silicon substrate. Using scanning electron microscope (SEM) imaging, the zinc oxide product morphology was analyzed. Small ‘nanonails’ were found to have grown on the substrate, with the stem diameter of the nails varying with position on the substrate. A simple, two-dimensional CFD model was then developed to investigate the concentration of each component gas (oxygen and zinc) at various locations in the reactor. Correlations were then drawn between the concentrations and the size of the stems on the nanonails produced, which provides some insight into how the process might be optimized for ideal control of the product.

A similar experiment was performed using an aerosol process to fabricate zinc oxide [16]. A solution containing zinc was aerosolized and pumped through a tube furnace. The zinc oxide particles produced by this process were collected at the exit of the tube furnace and inside a flask collector. A CFD model of the interior of the reactor was developed in order to determine internal temperature and flow velocity for each experimental run (see Figure 8 below). Zinc oxide particle morphology was analyzed via XRD and SEM and correlations were drawn between experimental parameters and product nanostructures.

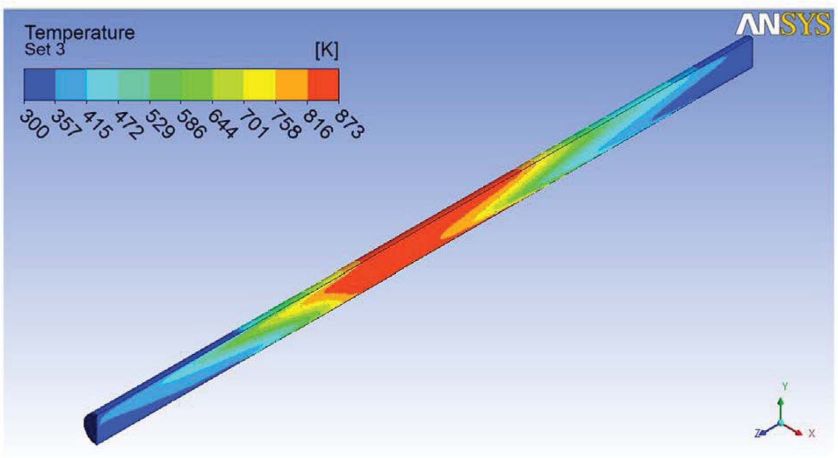

Figure 8 - CFD model of aerosol synthesis of zinc oxide showing temperature variation along the interior of the tube furnace [16]

In the following chapters, an experimental procedure is put forth and described, the products of the experiment are analyzed and characterized using SEM analysis, a CFD model of the experiment and its results are presented, and correlations are drawn between the conditions during the CVD process and the resulting nanostructures. Finally, possible applications of these findings are discussed.

Chapter 2: Experimental Procedure

2.1 Overview

A simple process was developed for the synthesis of zinc oxide nanostructures. A basic schematic of the experimental setup can be seen below in Figure 9. Zn metal powder (e in the figure) was placed on a copper support (d) and placed in the center of the tube furnace (a). Air was pumped through the tube, from the entrance (b) to the outlet (c). The silicon substrates (f) were placed downstream of the zinc powder.

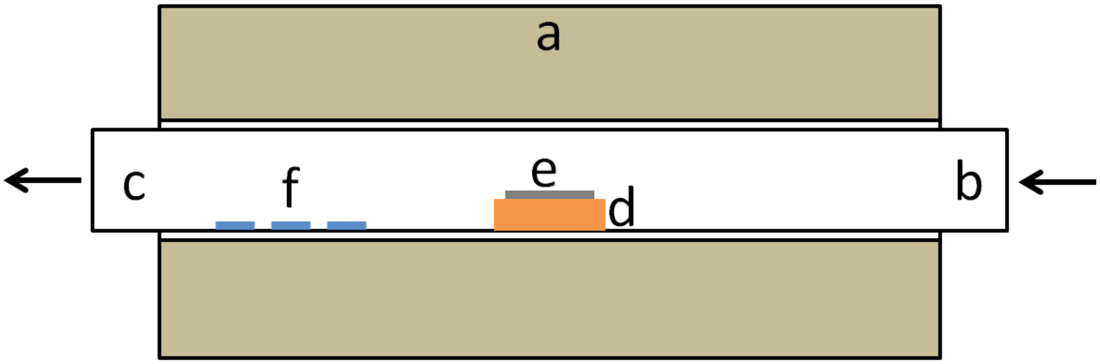

Figure 9 – Schematic of experimental setup

By heating the furnace while allowing a controlled amount of air to flow through the tube, the zinc would evaporate, flow down the length of the tube, and react with the oxygen in the air and deposit on the substrate.

2.2 List of Equipment

A list of the equipment used in this experiment can be found below:

- Plasma Cleaner (Fischione Model 1020)

- Sputter-coater (Polaron Instruments SEM Coating Unit E5100)
- Vacuum pump (Fisher Scientific Maxima C Plus)
- Pressure gauges (Varian Type 0531)
- Vacuum gauge (Varian Ratiomatic 843 Vacuum Ionization Gauge)
- Tube furnace (Thermolyne Type 21100)
- Leak valve (Edwards LV10K Fine Control Leak Valve)
- Thermocouples (K- and J-type)
- Data acquisition card (National Instruments NI 9213)
- LabVIEW (ver. 2014 SP1)
- FE-SEM (JEOL JSM-7600F)
- XEDS system (EDAX Octane Silicone Drift Detector and TEAM EDS software)

2.3 CVD Reactor Instrumentation

2.3.1 Furnace and Vacuum System

The furnace used for this experiment was a Thermolyne Type 21100 with an alumina tube (length of 91 cm, inner diameter of 3.175 cm, and outer diameter of 3.81 cm). The tube was connected at one end to a vacuum pump (Fisher Scientific Maxima C Plus) and to a leak valve (Edwards LV10K) on the opposite end. Pressure gauges (Varian Type 0531) were located at each end of the tube and were connected to a vacuum gauge for displaying the pressure at the inlet and outlet of the reactor. This setup allowed for pressure control via the leak valve. With the leak valve completely shut, a vacuum pressure of 13.33 Pa (10 mTorr) could be reached. Flow control was achieved by adjusting the leak valve to allow air to flow through the furnace, and inlet and outlet pressures were used to gauge the flow rate during experimentation.

2.3.2 Exterior Thermocouples

The temperature at various locations was measured via K- and J- type thermocouples, positioned on the outside of the tube as well as the tube interior, and temperature data was logged with a data acquisition card via a LabVIEW VI. Exterior thermocouples were mounted in groups of four at three locations of interest: the middle of the tube furnace, 11.4 cm downstream of the midpoint, and 22.8 cm downstream of the midpoint. At each location, a thermocouple was positioned at the top, bottom, front and back of the tube's exterior. The thermocouples were then held in place with wraps of thermocouple wire as shown in Figure 10, and the tube furnace with all 12 thermocouples installed can be seen in Figure 11.

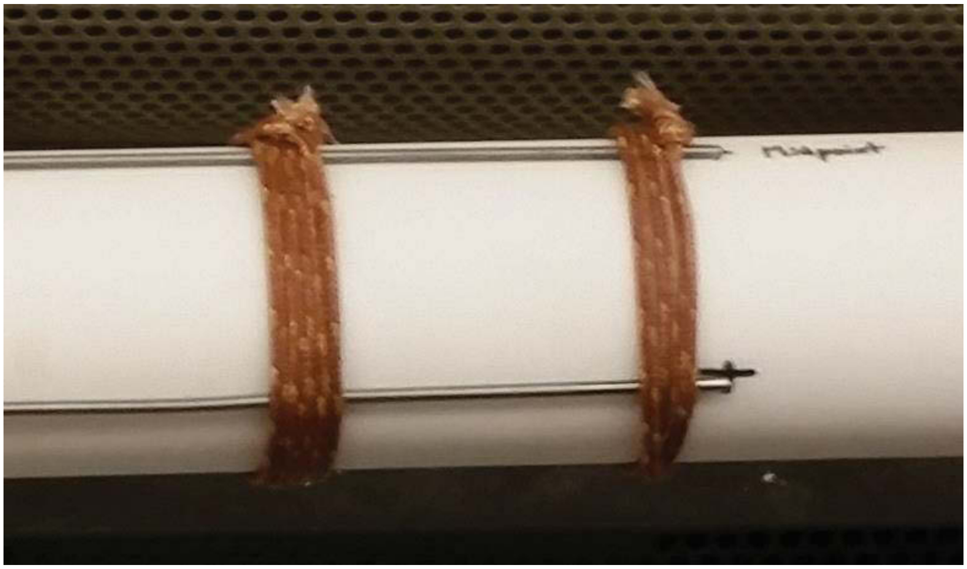

Figure 10 – Exterior thermocouples fastened to tube with thermocouple wire

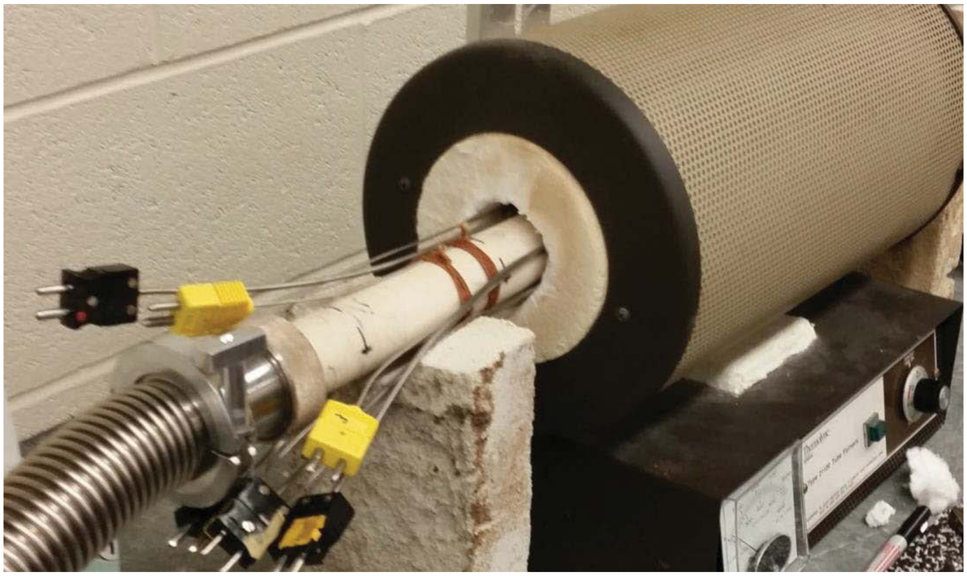

Figure 11 - Installed exterior thermocouples

2.3.3 Interior Thermocouples

Temperature inside the reactor was monitored via 4 k-type thermocouples with length of 61.0 cm and diameter of 0.508 mm. These particular thermocouples were selected because they would be able to reach into the middle of the furnace and be thin enough to avoid obstructing the flow within the furnace. A thin diameter was important for monitoring temperature without disrupting the flow within the furnace. In order to install the thermocouples, a hole was drilled in one of the fittings connected to the tube furnace. The thermocouple probes were fed into the furnace and bent such that they were spread across the cross-section of the tube. The hole was then resealed with vacuum epoxy. These thermocouples were used primarily for the purposes of verifying the CFD model and ensuring that simulated interior conditions matched the experimental interior conditions. The internal thermocouples can be seen in Figure 12 and Figure 13.

Figure 12 - Interior thermocouples and fitting

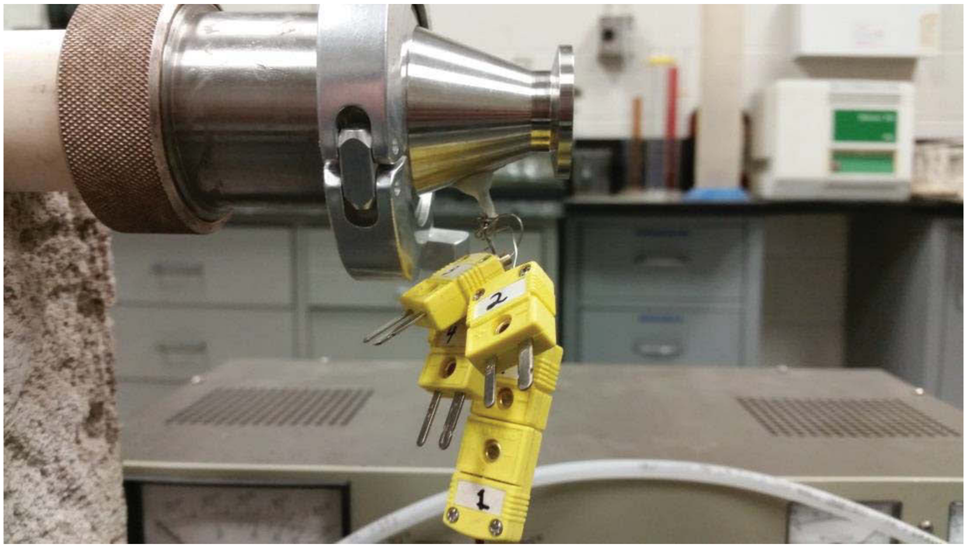

Figure 13 - Interior thermocouple hole sealed with epoxy

2.3.4 Temperature Recording

Temperature readings were logged with a LabVIEW VI connected to a data acquisition card. Temperature readings in °C were logged in 1 minute increments for the duration of each experiment in order to monitor experimental conditions, which were used to monitor ongoing experiments and were eventually used in the computational fluid dynamics calculations. The LabVIEW VI used was a simple loop which was set to record all temperature values at a user-selected frequency then write the results to a spreadsheet. The complete experimental setup can be seen below in Figure 14.

Figure 14 - Experimental Setup

2.3.5 Copper Boat

A copper boat was selected to hold the zinc metal powder used in the experiment. At low pressures, convection serves as a poor method of transferring heat, so it was decided that a conductive metal support should be machined which contacted the inside of the tube as much as possible. Copper was selected as a material because of its high heat conductance, which would ensure that a heat flux applied to the exterior of the furnace would be conducted through to the zinc metal. A notch was machined out of the bottom of the boat in order to allow the interior thermocouples to run underneath the boat while allowing the boat to maintain contact with the tube surface. The boat can be seen in Figure 15.

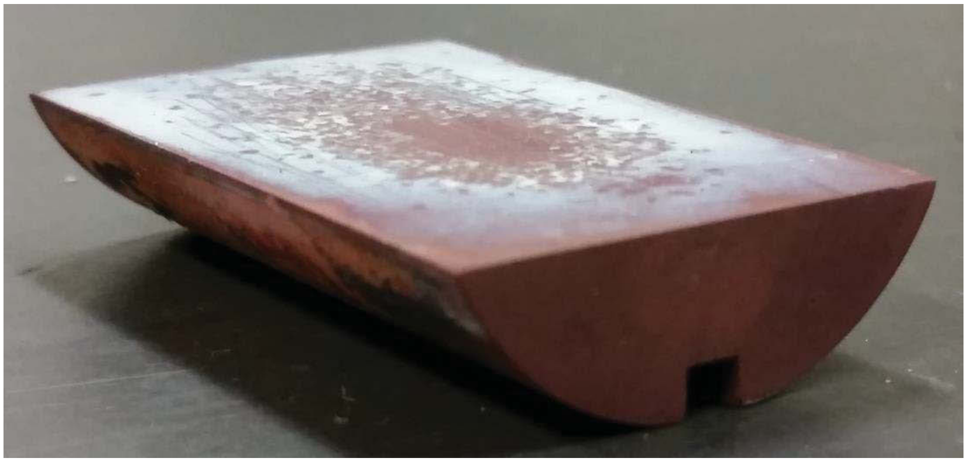

Figure 15 - Copper boat

2.4 Electron Microscopy Instrumentation

A JEOL JSM-7600F field emission scanning electron microscope (FE-SEM) was used to investigate the morphology and chemical composition of the materials used and obtained in the research. The instrument has the following basic parameters: 1 nm resolution at 15 kV, acceleration voltage range from 100 V to 30 kV, and probe current up to 2x10-7 Amps. The instrument is equipped with secondary electron detectors (conventional in-chamber and through-the-lens detectors), and a solid state backscattered electron detector. The instrument is also equipped with an EDAX Octane silicon drift detector for X-ray energy dispersive spectrometry (XEDS) chemical analysis. The silicon drift detector has an energy resolution of 129 eV guaranteed for Mn Kα. The XEDS data analysis is performed using EDAX TEAM EDS system.

2.5 Experimental Procedure

2.5.1 Substrate Preparation

Silicon wafers were prepared for use as substrates by using a three-part process: normal cleaning, plasma cleaning, and sputter-coating. The normal cleaning process was for removing bulk contaminants such as dust and oils from the substrate surface. The normal cleaning procedure consisted of the following steps:

1. Acetone wash at 90 °C for three minutes
2. Propanol wash at 90 °C for three minutes
3. Rinse with deionized water
4. Air dry

At the end of the process, each substrate was inspected via a light microscopy to make sure the surface was free of bulk contaminants. After inspection, the substrate was stored in weighting paper for storage and transport until further cleaning could be administered.

On the same day that deposition was to take place, plasma cleaning was conducted, using a Fischione Model 1020 plasma cleaner (Figure 16). The plasma cleaning step was implemented in order to eliminate molecular-scale contaminants on the surface of the substrate. The gas used by the cleaner to produce the plasma as per the manufacturer’s instructions was a mix of 75% argon and 25% oxygen by volume. Cleaning was conducted for a total of 30 minutes, after which each substrate was placed again in weighting paper for transport.

Figure 16 - Fischone Model 1020 Plasma Cleaner

Figure 17 - Plasma cleaner sample holder with silicon substrates

Immediately after the plasma cleaning procedure was completed, the substrates underwent sputter-coating in order to coat their surface in a gold-palladium film, which served as a catalyst for the CVD process. The sputter-coating process was conducted at room temperature. The instrument used for substrate coating was a Polaron Instruments E5100 SEM Coating Unit (Figure 18).

Figure 18 - Polaron Instruments E5100 sputter-coater

The substrates each had half of their surface covered in aluminum foil. This caused the Au-Pd film to form only on half of the substrate so that half of the substrate surface was bare silicon surface and the other half was coated in a film of Au-Pd. After 3 minutes of sputter-coating, the substrates were removed. To finalize the substrates, a drop of binder used in binder-jet additive manufacturing was added to a corner of the Au-Pd side of the substrate. This was done in order to introduce carbon into the system so that effects that carbon might have on the deposition might be investigation. After substrates were prepared, they were taken to the scanning electron microscope for pre-deposition characterization.

2.5.2 Vapor Deposition Experiment

The vapor deposition procedure itself began with measuring out the amount of zinc powder to include. A balance was used to measure the mass of the zinc metal powder on weighing paper and then the zinc was placed on the top surface of the copper boat. The mass of the zinc metal powder used in the experiment can be found in Table 1. Next, the ends of the interior thermocouples were inserted into the tube and the boat was carefully placed over the thermocouple wires. The wires and boat were then gently pushed into the tube furnace. Once the copper boat was in the dead center of the tube, the fitting holding the interior thermocouples was connected to the tube furnace, and the inlet side of the apparatus was attached.

The next step in the process was the loading of the substrates into the tube furnace. The outlet side of the tube was opened and the substrates were loaded into the alumina tube. Substrates were pushed down the tube a set distance which changed depending on the experiment being run. Exact measurements can be seen in Table 1. Substrate orientation had to be considered because the substrate surface was divided into sections based on surface preparation. The orientation of the substrates for the experiment can be seen in Figure 19.

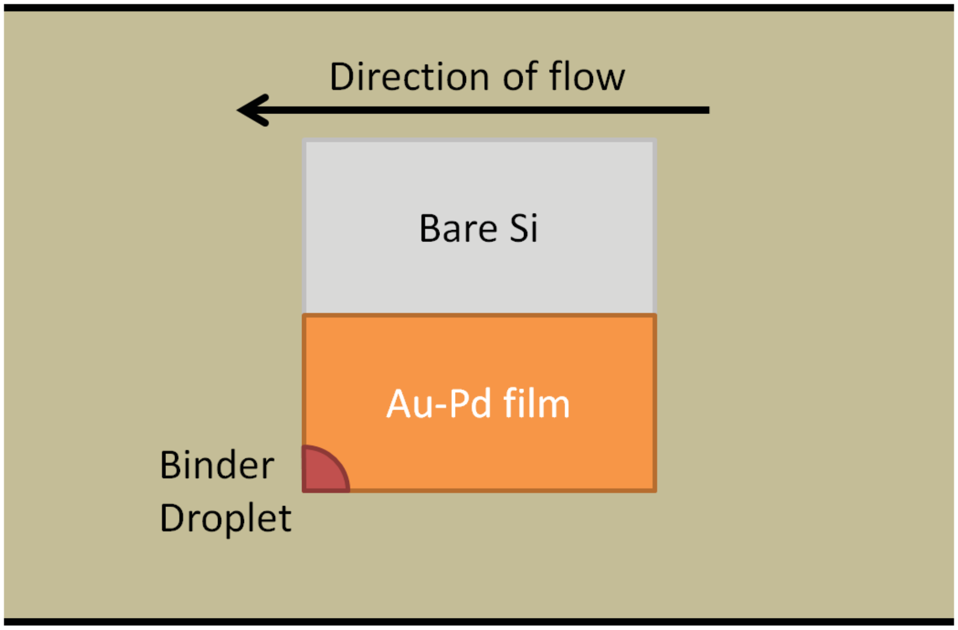

Figure 19 - Top-down view of substrate orientation for experiment

Once the substrates were fully inserted into the furnace, the outlet side of the tube was sealed to the vacuum pump, and the pump was started in order to evacuate the tube furnace. While this was occurring, the thermocouples were connected to the appropriate data acquisition cards and the LabVIEW VI was opened. Recording of temperature measurements was started once the VI had fully loaded. Recording the thermocouple readings at room temperature was important for later error calculations. When the pressure inside the tube furnace reached its lowest pressure (1.33 Pa), pressure readings for both inlet and outlet were recorded (once again for the purpose of error analysis), the furnace was turned on. Once the temperature exceeded 800 K, the leak valve was opened in order to allow air to flow through. The leak valve was set such that the desired inlet pressure of 13.33 Pa (100 mTorr) was maintained throughout the entire experiment. The experiment was then allowed to run for five hours.

At the end of the allotted time, the leak valve was shut in order to stop the flow of air through the system and the furnace was shut off. Temperature recording was terminated, and the furnace was allowed to cool down while retaining vacuum. Only after the system had returned to room temperature was air allowed to return to the system, after which the furnace was opened and the substrates were carefully removed for analysis.

Table 1 - Setup parameters for experiment

	Parameter Value
Zinc metal mass (g)	1.363 g
Substrate 1 positioning (mm from outlet)	362 mm
Substrate 2 positioning (mm from outlet)	352 mm
Pressure at inlet (Pa)	13.33 Pa (100 mTorr)
Centerline Temperature	800 K
Run Time	5 hours

2.6 Error Analysis

Error analysis was conducted using data recorded during the experiment. Pressure gauge bias was determined by comparing readings at vacuum. Temperatures were recorded for some time prior to turning on the furnace and this data was used in order to compute the bias for each individual thermocouple. The precision error was determined by performing statistical analysis on the temperature readings at maximum furnace temperature. Student’s t-distribution was used with a sample size of 200 and a confidence interval of 95%. Total errors were determined by the root sum squares method. All error quantities can be seen in Table 2.

Table 2 – Error Analysis

		Bias Error	Precision Error (95% confidence)	Total
Pressure	Inlet	0.133 Pa		0.133 Pa
	Outlet	-0.133 Pa		-0.133 Pa
Temperature				
Inner	Top	-0.0648 K	2.566 K	2.567 K
	Back	-0.0400 K	2.565 K	2.566 K
	Front	-0.0819 K	2.564 K	2.565 K
	Bottom	-0.0964 K	2.574 K	2.576 K
Middle	Top	-0.0719 K	2.664 K	2.665 K
	Back	-0.1072 K	2.692 K	2.694 K
	Front	-0.1674 K	2.661 K	2.667 K
	Bottom	-0.1727 K	2.671 K	2.677 K
Outer	Top	0.0164 K	1.579 K	1.579 K
	Back	-0.0836 K	1.645 K	1.647 K
	Front	0.1109 K	2.748 K	2.751 K
	Bottom	-0.2013 K	3.985 K	3.990 K
Interior	1	0.1716 K	2.604 K	2.610 K
	2	0.2026 K	2.583 K	2.592 K
	3	0.2774 K	2.601 K	2.615 K
	4	0.3084 K	2.612 K	2.630 K

Chapter 3: Numerical Setup

3.1 Software Selection

For this work, ANSYS Fluent and ICEM CFD meshing were selected for all simulations. Fluent was chosen because of its availability to perform simulations in two dimensions as well as three dimensions. ICEM CFD meshing was chosen for the large degree of control it grants the user when creating and refining the mesh. Because the geometry of this experiment was fairly simple, meshing could be carefully controlled by hand in order to produce a high quality mesh with a small element count. Using these software packages, both two-dimensional and three-dimensional models were developed and run.

3.2 Geometry

The geometry involved in this model was quite simple. The reactor itself contains only two objects of notable size: the copper boat and silicon substrate(s). In order to represent the evaporation of the zinc metal, an additional volume was considered: a zone above the copper boat which would serve as a source region to introduce zinc vapor into the system. In all, creation of the geometry used in both analyses was straightforward.

The two-dimensional geometry was developed using ANSYS DesignModeler version 16.1. The model geometry simply consisted of a body made of a variety of straight lines. This basic geometry was imported into ICEM CFD, where each line was assigned a part name which corresponded to the boundary condition it represented (e.g. wall, inlet, outlet). No surfaces needed to be created prior to meshing, as the fluid and solid interiors were generated as a part of the meshing process. A detail view of the basic geometry of the two-dimensional model can be seen in Figure 20.

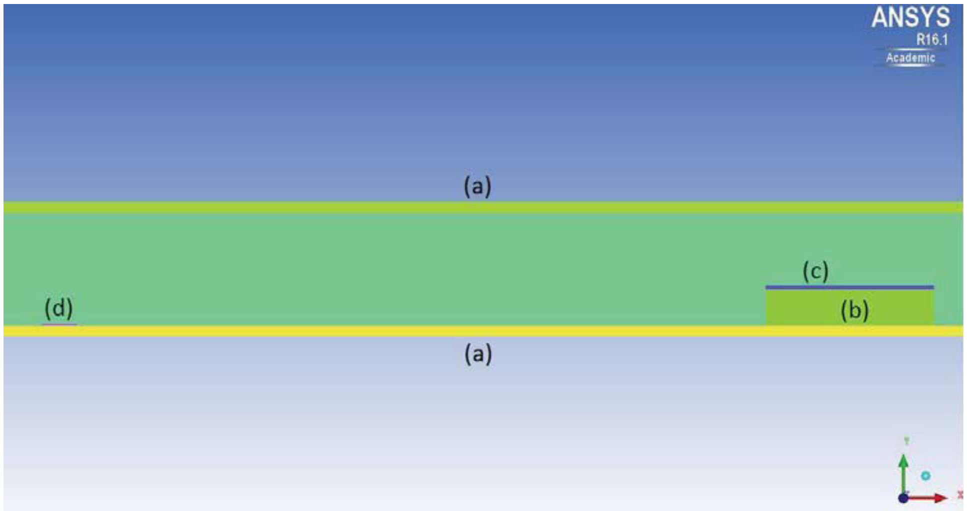

Figure 20 - Two-dimensional CFD geometry. (a): tube walls, (b) copper boat, (c) zinc source region, (d) substrate

The three-dimensional geometry was created in SolidWorks 2015. It was decided that symmetry along the vertical plane should be utilized in order to save on computation time. The model consisted of the reactor tube, the copper boat, the silicon substrate, and a source region directly above the copper boat (Figure 21). Some concessions were made in order to ensure that a good quality mesh could be produced. Specifically, geometry was altered for the silicon substrate. The 0.5 mm thick silicon wafer, in reality, has a small clearance between its bottom surface and bottom wall of the tube. Furthermore, the substrate only contacts the tube wall along its edges, meaning that a quad-based mesh will produce low quality elements around the junction. The substrate was instead approximated as having a curved bottom, with a radius of curvature the same as the inner radius of the alumina tube. An illustration of this compromise can be seen in Figure 22.

The SolidWorks model was saved as a parasolid file and imported into ANSYS. ICEM CFD was then used to assign part names to each piece of geometry in accordance to the boundary condition it served to represent.

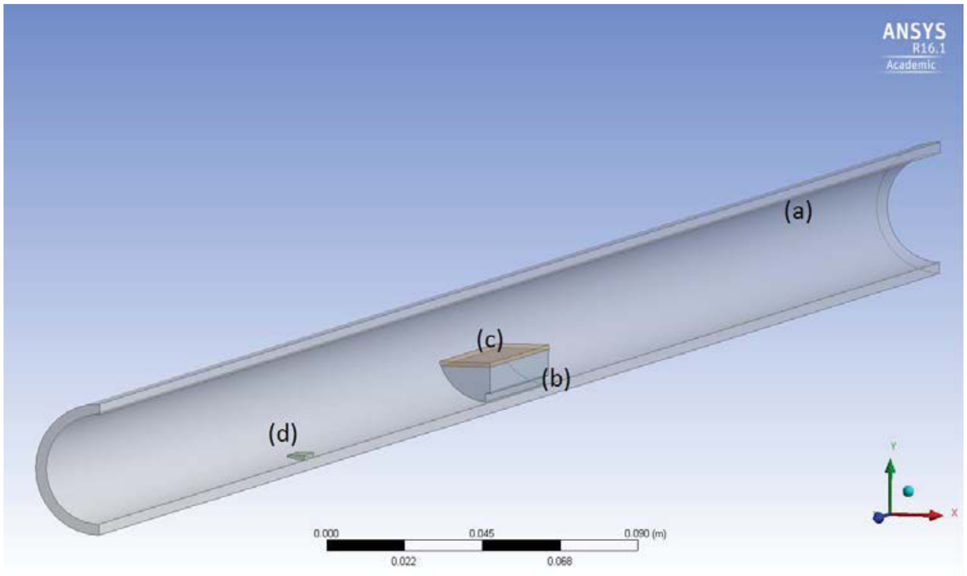

Figure 21 - Three-dimensional CFD geometry. (a): alumina tube, (b): copper boat, (c): zinc source zone, (d): silicon substrate

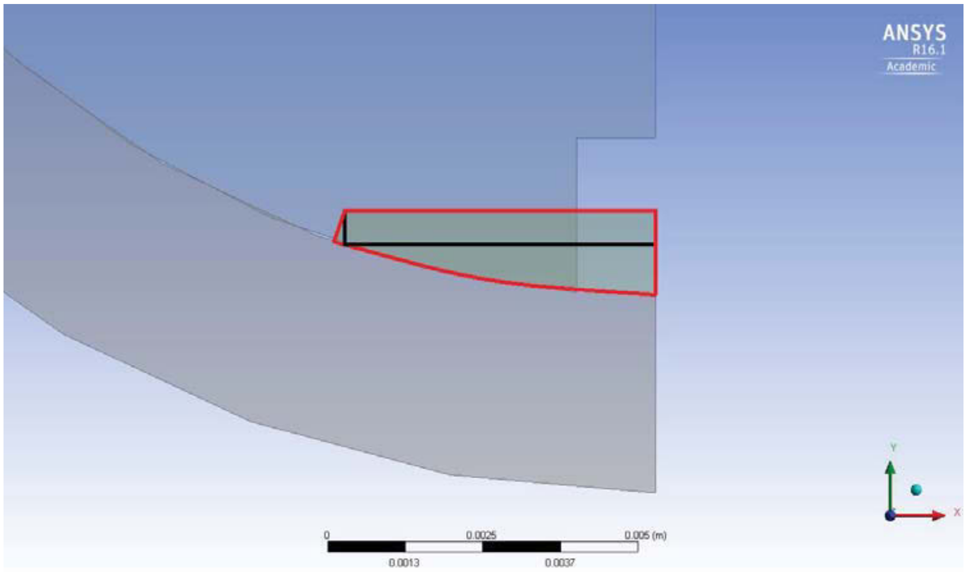

Figure 22 - Substrate geometry approximation. Actual geometry outlined in black, approximated geometry outlined in red

3.3 Meshing

Meshing was, as mentioned earlier, conducted in ICEM CFD. The general process followed for both models was to create an overall block, then split to fit each part in the model, and finally associate the blocks, placing priority on fixing points, then edges, then surfaces. Once full association was accomplished, a pre-mesh was generated and the mesh was inspected for errors in association. Mesh size was controlled via ICEM CFD's edge property management tools. A smooth transition between regions of differing element densities was accomplished by linking the edges of adjacent regions and setting the transition ratio to 1.2 as opposed to the default setting of 2. This meant that the cells in a less dense region began roughly the same size as the smaller cells in the adjacent region, but each successive cell was 1.2 times larger than the previous one, so that the transition between regions was smooth. A smooth transition in element size is important for achieving maximum accuracy in a simulation, so this parameter was important. Once a mesh had been produced, boundary condition types were assigned to each part of the model, and the mesh was exported to Fluent for setup and simulation.

3.4 Simulation Parameters

Because the synthesis process is driven entirely by temperature differences and evaporation of a metal powder, both the energy equation and species transport models were enabled. The SIMPLE Pressure-Velocity coupling method was chosen, and second-order discretization schemes were used for continuity, momentum, and energy equations.

3.5 Material Properties

The experiment being simulated in this CFD analysis was reliant on thermal conditions as well as the evaporation of a metal and its mixing with a carrier gas. For these reasons, the energy equation was added to the model, as was species transport. Thus, the variation of properties with respect to temperature has to be considered.

All solid material properties were taken from the ANSYS material library. The properties of the fluids involved in the simulation came from other sources. While the ideal gas assumption would have been applicable for modeling this process (low pressures, high temperatures), it was not used to determine fluid densities in order to reduce the complexity of the simulation. Instead, a polynomial best fit for air and zinc vapor densities were developed based upon density data from the ideal gas assumption. Air viscosity, specific heat, and thermal conductivity were derived from polynomial relations. Çengel and Boles [17] provided the specific heat polynomial, and Kadoya *et al*. [18] provided polynomial relations for both viscosity and thermal conductivity based on both temperature and density of air. These polynomials can be seen in Table 3 through Table 7. The average properties of air in the reactor were determined based upon early experimentation, then a constant value was computed for thermal conductivity, viscosity, and specific heat of air.

Table 3 - Air Density and Specific Heat

Property	Relation
Density (kg/m^3)	$\rho = 6.570 * 10^{-4} - 3.492 * 10^{-6} * T + 8.187 * 10^{-9} * T^2 - 8.804 * 10^{-12} * T^3 + 3.557 * 10^{-15} * T^4$
Specific Heat (J/kg-K) as a function of temperature (K)	$\bar{c_p} = 970 + 0.06792 * T + 1.658 * 10^{-4} * T^2 - 6.789 * 10^{-8} * T^3$

Table 4 - Air Viscosity Relations [18]

Total Dynamic Viscosity (Pa*sec)	$\eta(T_r, \rho_r) = \mathrm{H}[\eta_0(T_r) + \Delta\eta(\rho_r)]$
Low Pressure Viscosity	$\eta_0(T_r) = A_1 T_r + A_{0.5} T_r^{0.5} + \sum_{i=0}^{-4} A_i T_r^i$
Excess Viscosity	$\Delta\eta(\rho_r) = \sum_{i=1}^{4} B_i \rho_r^i$
	$T_r = \frac{T}{T^*}$
	$\rho_r = \frac{\rho}{\rho^*}$

Table 5 - Air Viscosity Relation Coefficients [18]

H^*	$6.16090 * 10^{-6}\ Pa * sec$
T^*	$132.5\ K$
ρ^*	$314.3\ \frac{kg}{m^3}$
A_1	0.128517
$A_{0.5}$	2.60661
A_0	-1.0000
A_{-1}	-0.709661
A_{-2}	0.662534
A_{-3}	-0.197846
A_{-4}	0.00770147
B_1	0.465601
B_2	1.26469
B_3	-0.511425
B_4	0.274600

Table 6 - Air Thermal Conductivity Relations

Total Thermal Conductivity (W/m-K)	$\lambda(T_r, \rho_r) = \Lambda[\lambda_0(T_r) + \Delta\lambda(\rho_r)]$
Low Pressure Thermal Conductivity	$\lambda_0(T_r) = C_1 T_r + C_{0.5} T_r^{0.5} + \sum_{i=0}^{-4} C_i T_r^i$
Excess Thermal Conductivity	$\Delta\lambda(\rho_r) = \sum_{i=1}^{4} D_i \rho_r^i$
	$T_r = \frac{T}{T^*}$
	$\rho_r = \frac{\rho}{\rho^*}$

Table 7 - Air Thermal Conductivity Relation Coefficients

Λ^*	$25.9778 * 10^{-3} \frac{W}{m * K}$
T^*	$132.5\ K$
ρ^*	$314.3 \frac{kg}{m^3}$
C_1	0.239503
$C_{0.5}$	0.00649768
C_0	1.00000
C_{-1}	-1.92615
C_{-2}	2.00383
C_{-3}	-1.07553
C_{-4}	0.229414
D_1	0.402287
D_2	0.356603
D_3	-0.163159
D_4	0.138059
D_5	-0.0201725

Zinc vapor properties are not well-documented, so the kinetic theory of gasses was used in order to approximate its behavior. Kinetic theory assumes an ideal gas and it makes predictions about fluid properties based upon particle parameters, which include characteristic length, an energy parameter, and the particle's degrees of freedom. The equations used to approximate dynamic viscosity and thermal conductivity can be seen below. Zinc vapor was assumed to be monoatomic, and so each particle possesses three degrees of freedom, one for each translational axis. Energy and length parameters were found in literature [19]. Density of zinc vapor was again assumed to be that of an ideal gas due to the high temperatures involved. Zinc vapor parameters can be seen in Table 8.

Table 8 - Zinc vapor parameters

Property	Parameter
Density (kg/m^3)	$\rho = 1.602 * 10^{-3} - 8.759 * 10^{-6} * T + 2.078 * 10^{-8} * T^2 - 2.248 * 10^{-11} * T^3 + 9.111 * 10^{-15} * T^4$
Molecular Weight (M_W)	65.38 kg/kmol
Characteristic Length Parameter (σ)	2.556 Å
Energy Parameter $\left(\frac{\varepsilon}{k_B}\right)$	1356 K
Degrees of Freedom (f_i)	3
Specific Heat Capacity	$c_p = \frac{1}{2}\frac{R}{M_W}(f_i + 2)$
Dynamic Viscosity	$\mu = 2.67 * 10^{-6}\frac{\sqrt{M_W T}}{\sigma^2 \Omega_\mu(T^*)}$
	$T^* = T * \frac{k_B}{\varepsilon}$
Thermal Conductivity	$k = \frac{15}{4}\frac{R}{M_W}\mu\left[\frac{4}{15}\frac{c_p M_W}{R} + \frac{1}{3}\right]$

Finally, properties of the mixture were computed based upon mixing laws. For both simulations, mass-based mixing laws were used to determine all parameters.

3.6 Boundary Conditions

Most boundary conditions used in this simulation were straightforward. All walls used the wall boundary condition and the symmetry boundary condition was employed along the Z-Y plane. The four most important boundary conditions were the inlet, outlet, wall temperature, and zinc source boundaries, which drove the simulation.

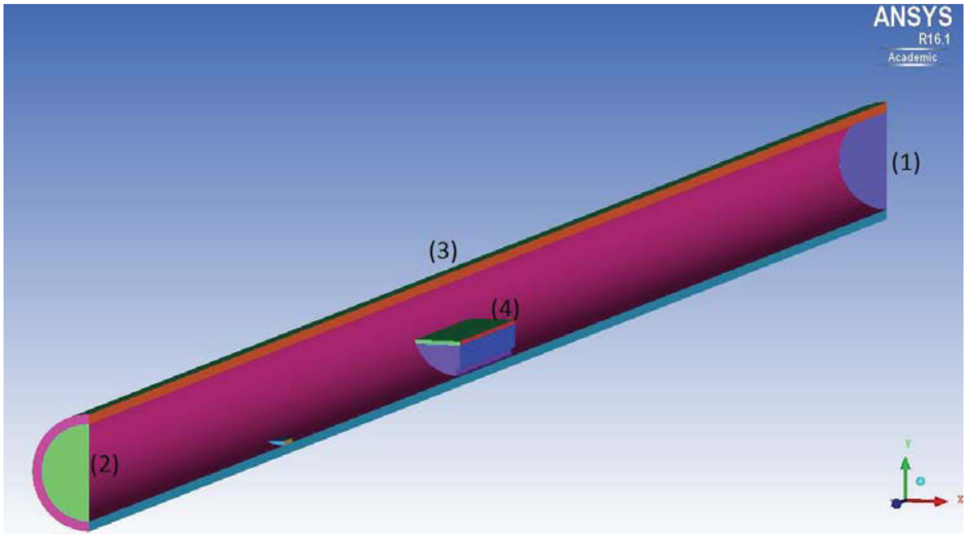

Figure 23 - Significant boundary conditions: (1) inlet, (2) outlet, (3) tube exterior, (4) zinc source

3.6.1 Inlet and Outlet

Inlet and outlet boundary conditions were selected based upon the experimental setup. Pressure boundary conditions were used at both inlet and outlet. The specific values were selected based upon the pressures measured at the inlet and outlet of the reactor during the experiment. Two sets of boundary conditions were developed: one corresponding to the experimental run and one representing an alternate set of experimental parameters. The temperature condition at inlet was set to room temperature based on experimental observations, and a mass fraction of 0 was enforced at the inlet for zinc vapor, representing pure air flowing into the reactor. The inlet and outlet boundary conditions can be seen below.

Table 9 - Inlet and Outlet Boundary Conditions

Parameter	Case 1	Case 2
Inlet Temperature	300 K	300 K
Inlet Mass Fraction of Zinc Vapor	0	0
Inlet Pressure	13.332 Pa (100 mTorr)	6.666 Pa (50 mTorr)
Outlet Pressure	10.666 Pa (80 mTorr)	5.333 Pa (40 mTorr)

3.6.2 Wall Temperature

As mentioned previously, temperature of the exterior walls of the alumina tube was measured via 12 thermocouples. This data was interpolated using a polynomial fit scheme in order to generate a smooth temperature profile. An excel spreadsheet was created which would map a position on the wall to the appropriate temperature. Each time a new mesh was brought into Fluent, the coordinates of the points along the exterior of the tube were exported as a profile. This profile was opened and imported into the Excel spreadsheet, and a temperature was assigned to each point. This data was then re-entered into Fluent in order to generate a smooth temperature gradient. An example of the temperature profile can be seen in Figure 24.

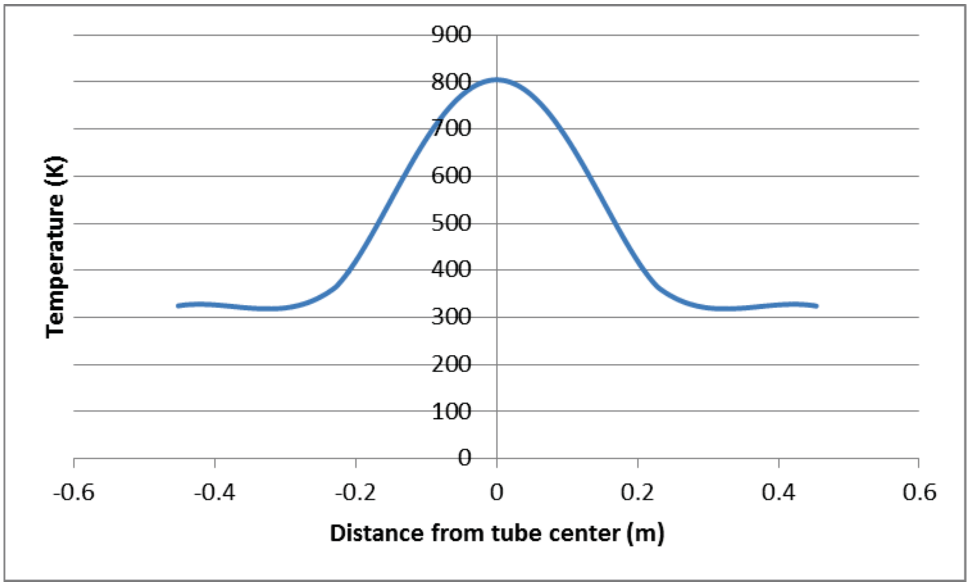

Figure 24 - Temperature boundary condition profile

3.6.3 Zinc Vapor Source

The zinc vapor source region of the model was used to simulate the evaporation of zinc metal powder. A source term was established, which meant that the model treated the zone as a region where a set amount of zinc vapor entered at a given rate. Based upon experimental measurements, zinc vapor was calculated to enter the system at a rate of 6.31e-5 kg/sec. Because the Fluent source term parameter accepts input in the form of mass per unit volume per second, the actual input varied between the two models. Relevant values and input can be seen in Table 10.

Table 10 - Source zone input calculation

	2D	3D
Source zone volume (m^3)	1.28 e-06	9.218e-7
Rate of mass creation (kg/s)	6.31e-5	6.31e-5
Mass source term (kg/s-m^3)	0.0493	0.06846

3.7 Grid Convergence

In any numerical analysis, it is possible that the coarseness of the mesh can impact the accuracy of the results. In order to prevent this, grid convergence testing was conducted. In grid convergence testing, the same simulation is conducted using a mesh of differing size. If the results in a location of interest are essentially the same for both simulations, then it can be said that the grid has converged. If they are different, then a refined mesh must be created and the simulation must be run again.

For these two models (2D and 3D), grid convergence was determined by two checks. The first check was the temperature profile along the top of the substrate. Specifically, the difference in temperature along the substrate's top surface was compared to determine convergence. The second check was the velocity profile across the tube at a location just upstream of the substrate. If both checks showed convergence, then the whole mesh was considered to be sufficiently fine. Grid convergence testing results can be seen in Table 11.

Table 11 - Grid Convergence Results

		Difference in temperature	Difference in velocity
2D	mesh 1: 20,445 elements	2.33%	0.01%
	mesh 2: 27,564 elements	Base	Base
	mesh 3: 36,999 elements	1.08%	0.02%
3D	mesh 1: 405,889 elements	3.15%	1.51%
	mesh 2: 515,726 elements	Base	Base
	mesh 3: 746,751 elements	1.87%	1.03%

3.8 Final Meshes

The final meshes for both 2D and 3D simulations are orthogonal and can be seen in Figure 25 through Figure 30. The detailed statistics for both can be seen in Table 12. Of particular note is the high element count for the final meshes. For a 2D simulation, a number closer to 10,000 elements is typically more appropriate, and a mesh size of over 500,000 elements would be considered excessive for even a 3D mesh. In this case, the high aspect ratio of the geometry itself forced the use of a higher element count. Having elements with a high aspect ratio results in poor simulation accuracy, thus a denser mesh is a necessity when dealing with the geometry in this case.

Table 12 - Final Mesh Statistics

	2D Mesh	3D Mesh
Element Count	27,564	515,726
Node Count	26,197	471,607

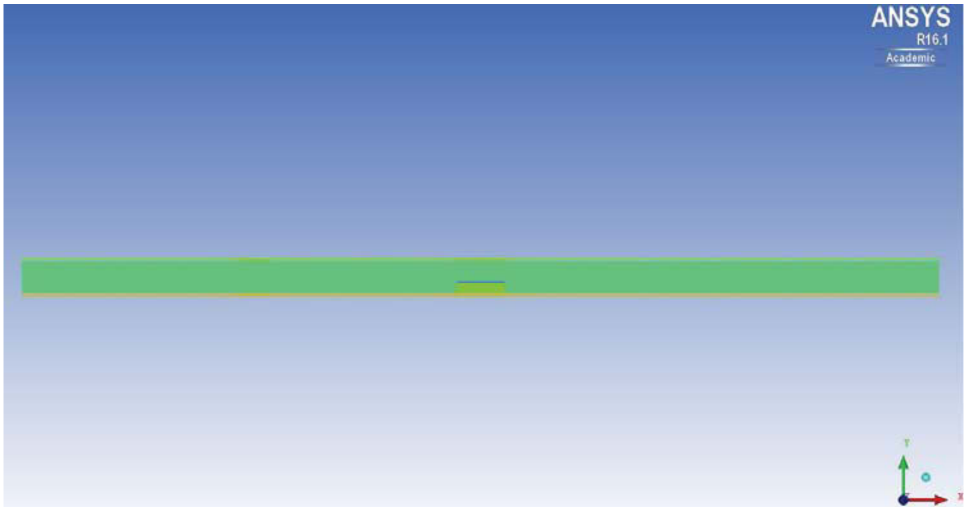

Figure 25 - Final 2D mesh

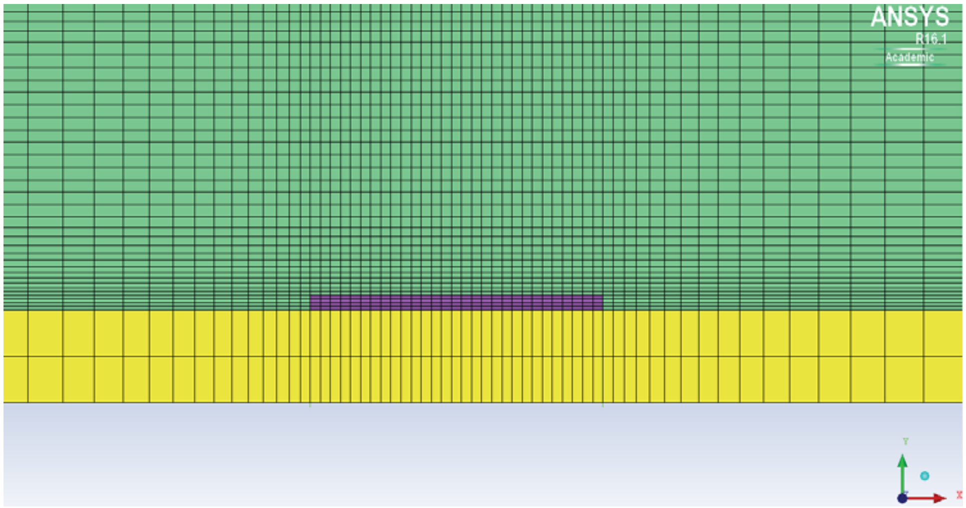

Figure 26 - Detail of substrate region on 2D mesh

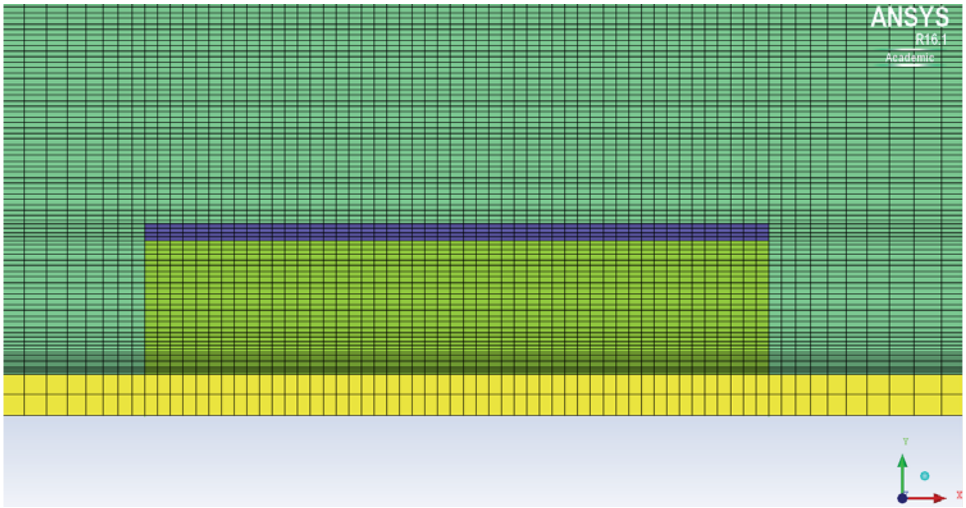

Figure 27 - Detail view of copper support and zinc source region on 2D mesh

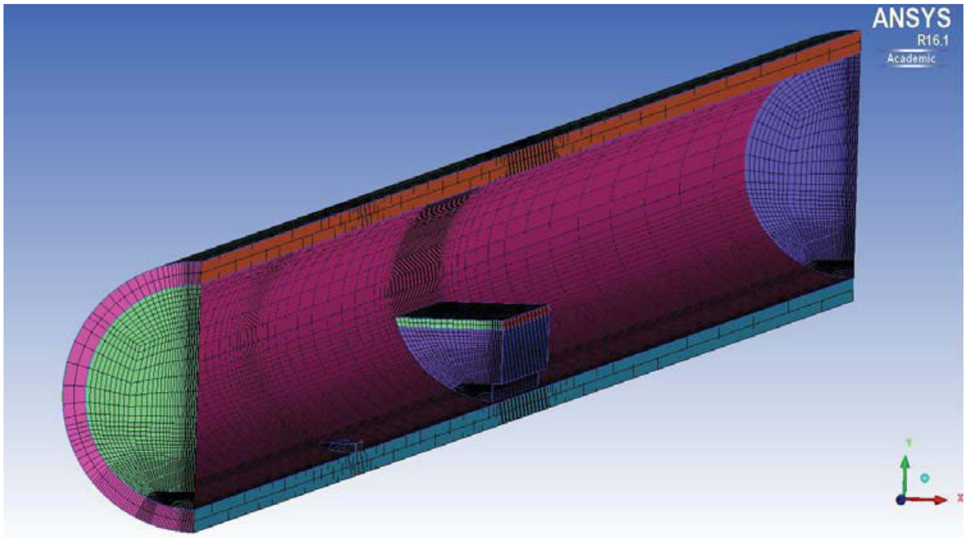

Figure 28 - Final 3D mesh

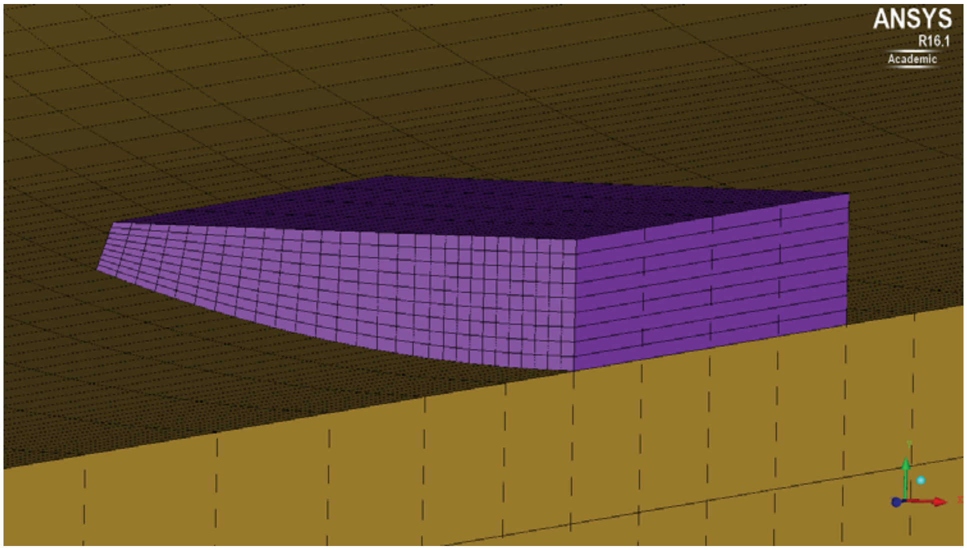

Figure 29 - Detail of substrate region on 3D mesh

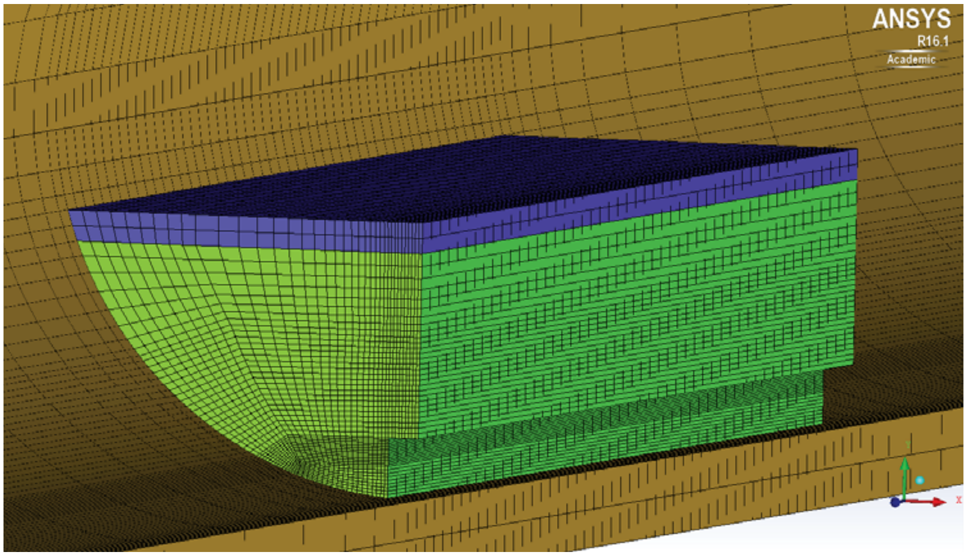

Figure 30 - Detail view of copper boat and zinc source region on 3D mesh

Chapter 4: Results and Discussion

4.1 Electron Microscopy Investigation of ZnO Nanostructures Obtained by CVD

Once the synthesis process was finished, the reactor was opened and the silicon substrates were carefully removed from the tube furnace. The interior thermocouples and copper support were removed from the furnace as well, and both showed signs of some zinc vapor deposition. The substrates and samples taken from the copper boat and thermocouples were all examined via SEM investigations. Chemical composition analysis of the obtained materials was performed in the SEM using X-ray energy dispersive spectroscopy (XEDS or EDS). Figure 31 shows the regions in which zinc oxide was discovered.

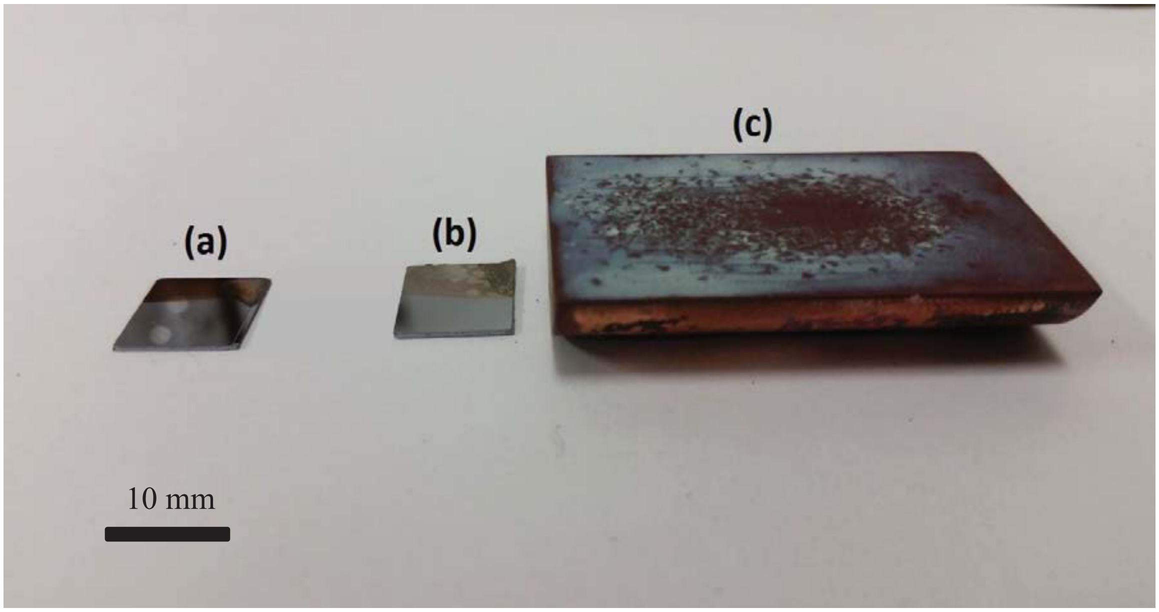

Figure 31 - Zinc oxide deposition sites. (a) – Outer Substrate, (b) – Inner Substrate, (c) – Unevaporated Powder

4.1.1 Silicon Substrate

Prior to the deposition, the silicon substrates were analyzed in order to characterize them and verify the chemical composition prior to the vapor deposition experiment. SEM analysis revealed the morphology of the Au-Pd coating on the substrate, and EDS analysis confirmed a surface composition of mainly silicon with amounts of gold, palladium, and carbon. The carbon presence could possibly be caused by wrapping the sample in weighing paper for transport. An SEM image of the substrate can be seen in Figure 32, the EDS spectrum can be seen in Figure 33.

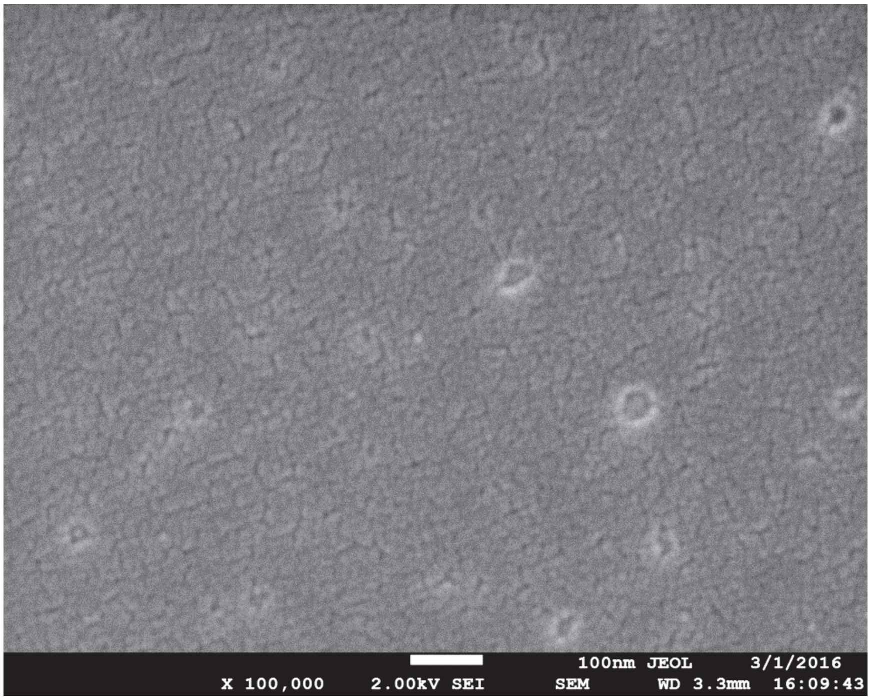

Figure 32 - Au-Pd coating on Si substrate.

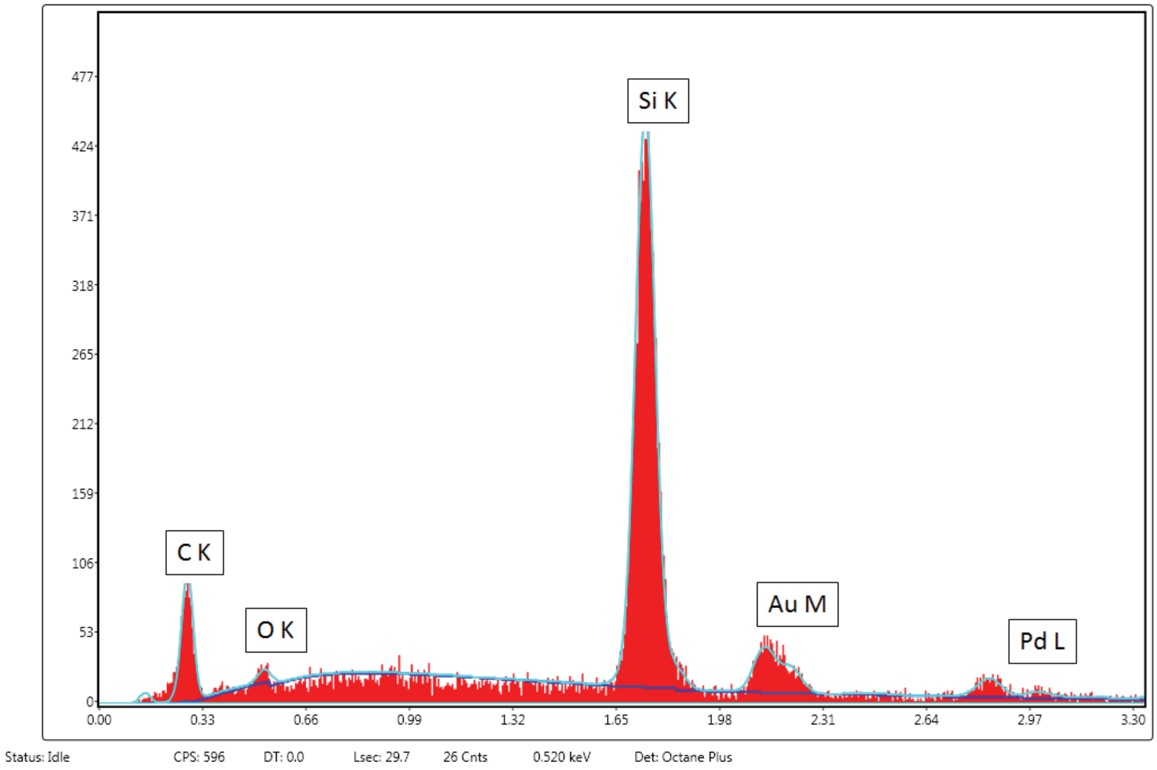

Figure 33 - EDS spectrum of Au-Pd coating on Si substrate.

4.1.2 Outer Substrate

The outer substrate was the substrate located closest to the outlet during the experiment. The bulk of the substrate surface consisted of largely unaltered Au-Pd, but isolated regions of zinc oxide deposition were found. Figure 34 shows one such region where zinc oxide nanowires formed. Closer inspection of the nanowires (Figure 35) shows that the wires grew from the catalyst, which became dislodged from the silicon surface. EDS analysis confirming the presence of zinc oxide can be seen in Figure 36.

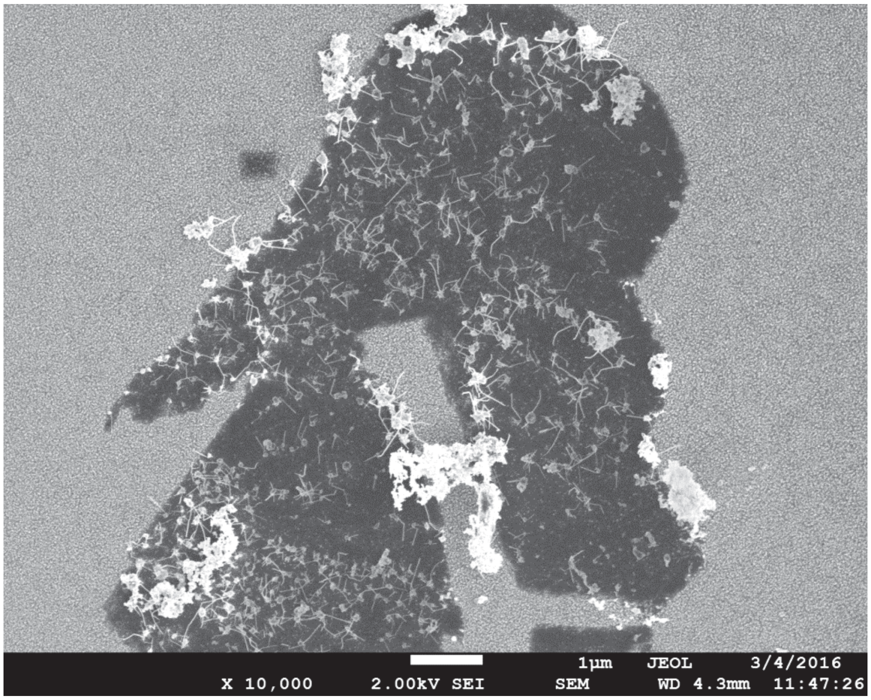

Figure 34 - Outer substrate nanowire growth

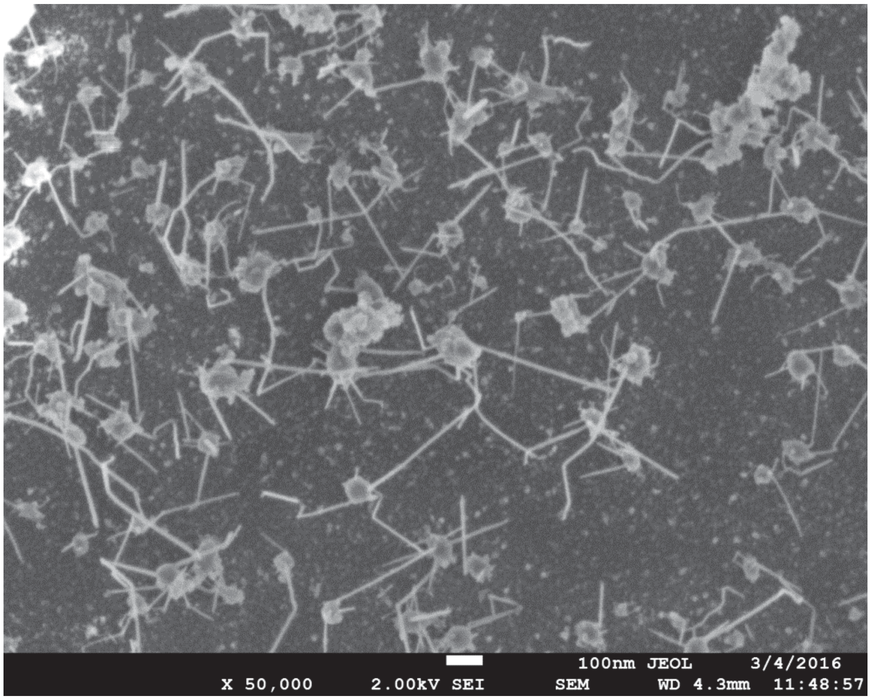

Figure 35 - Outer substrate nanowire growth, closer view

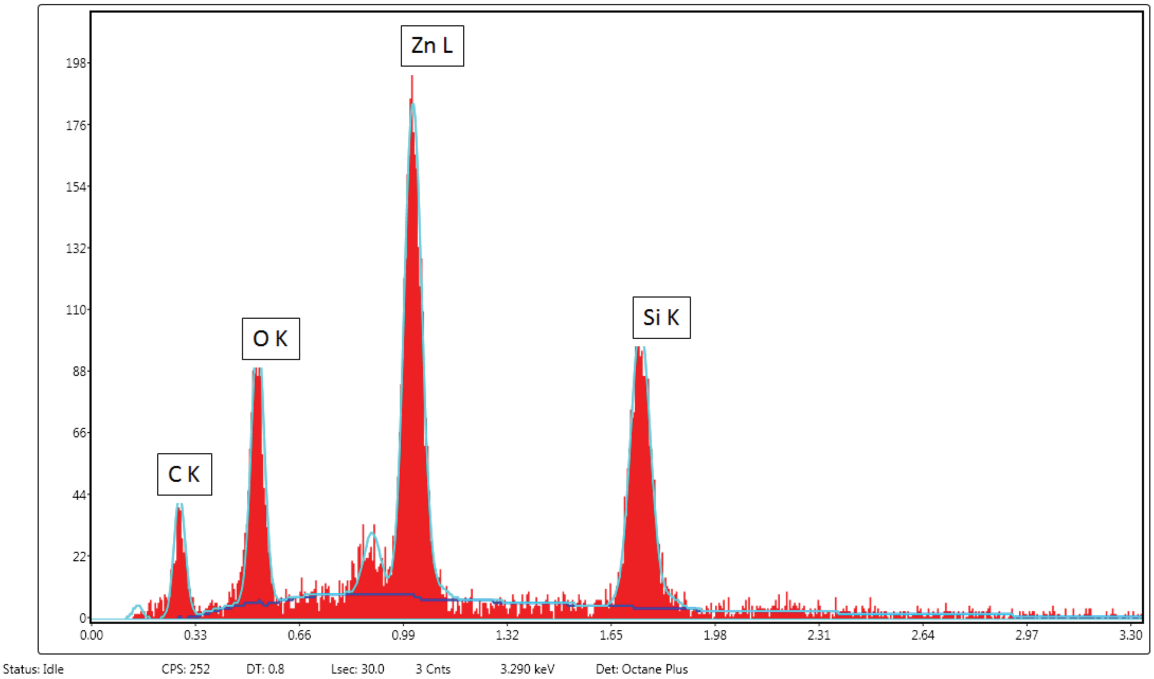

Figure 36 - EDS spectrum of outer substrate nanowire growth

In addition to the isolated patches of zinc oxide deposition, an inclusion was discovered on the substrate (Figure 37). As can be seen more clearly in Figure 38, the inclusion is covered in dense nanowire growth. EDS analysis was conducted in order to determine the chemical composition of this inclusion, as it seems to be a good catalyst for nanowire formation. The resulting spectrum, shown in Figure 39, revealed that the inclusion was largely zinc in composition.

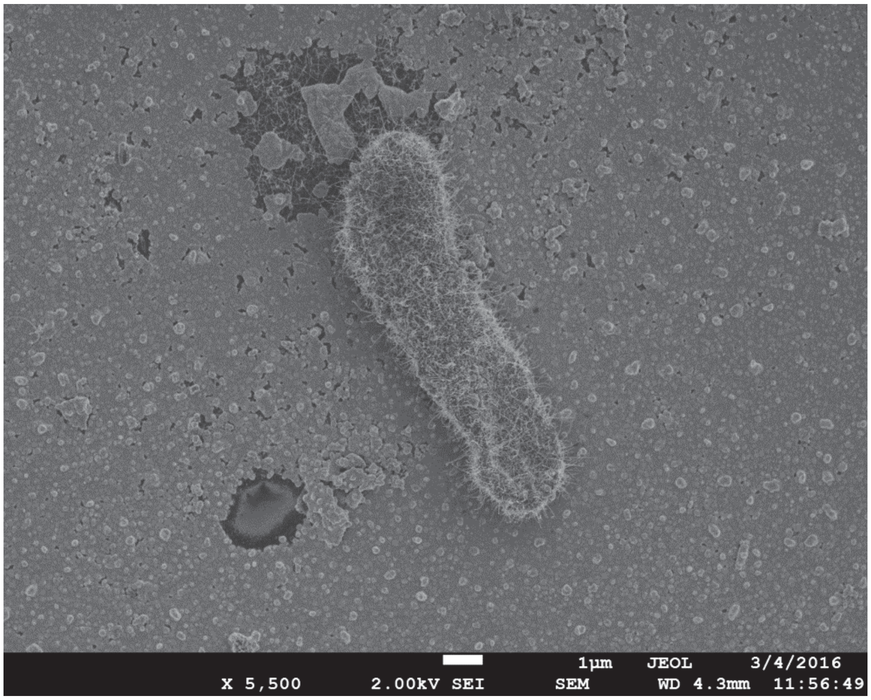

Figure 37 – Inclusion with nanowire growth on outer substrate

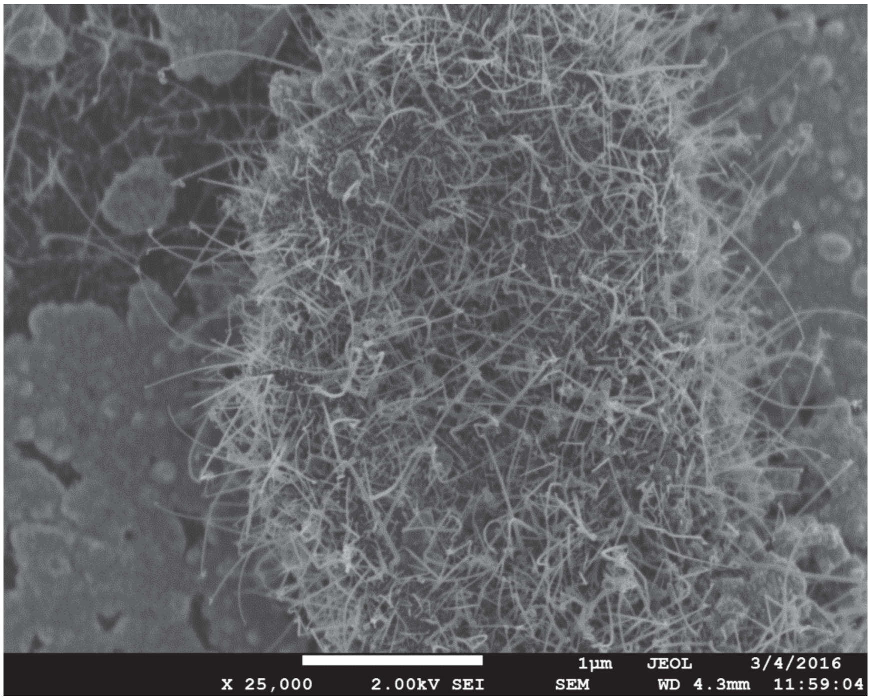

Figure 38 - Inclusion with nanowire growth on outer substrate, closer view

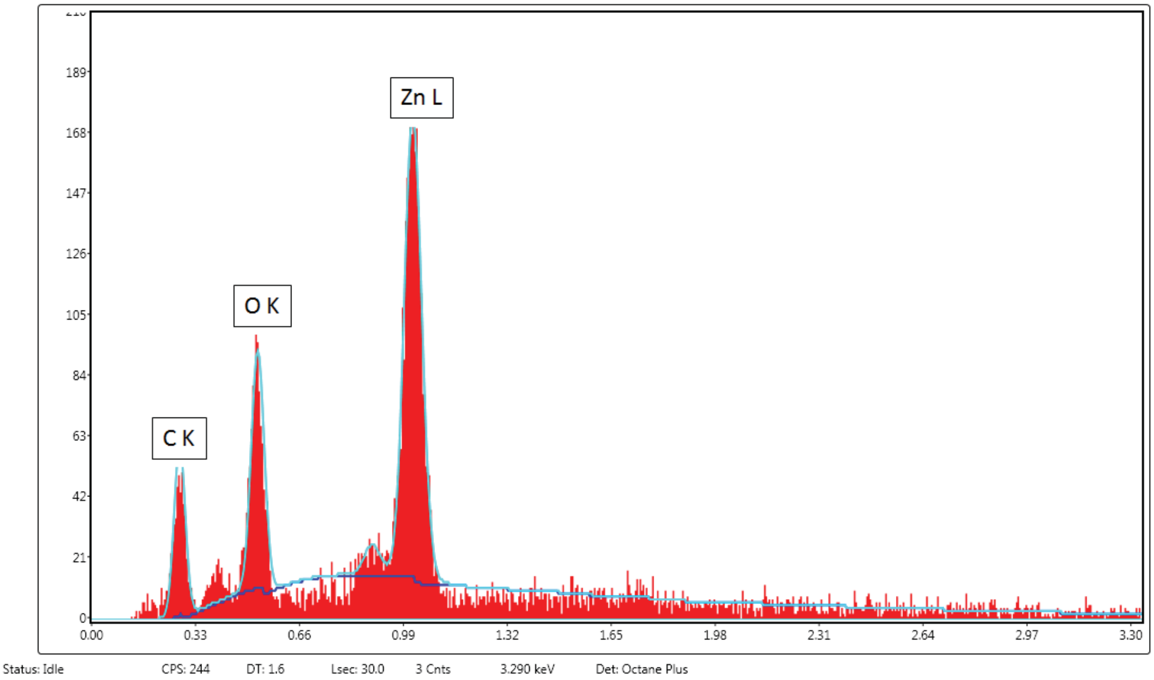

Figure 39 - EDS spectrum of inclusion on outer substrate

4.1.3 Inner Substrate

Examination of the inner substrate showed no signs of zinc oxide nanowire formation, but large single-crystal growths had formed on the surface of the substrate during the experiment (Figure 40 and Figure 41). Chemical analysis showed that the large crystals were a zinc-gold alloy, but the surrounding material was actually zinc oxide.

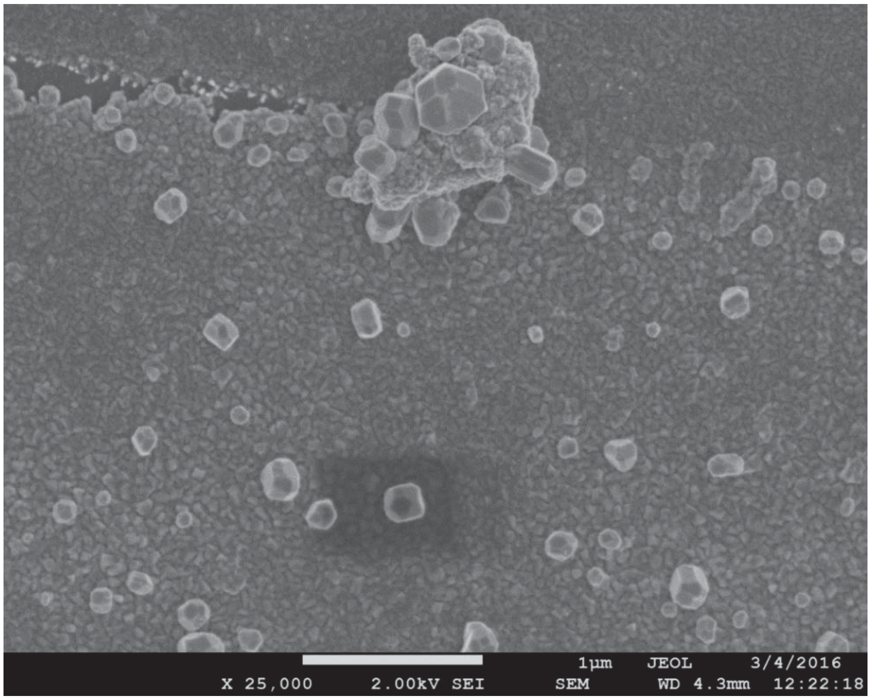

Figure 40 - Inner substrate surface morphology after experiment

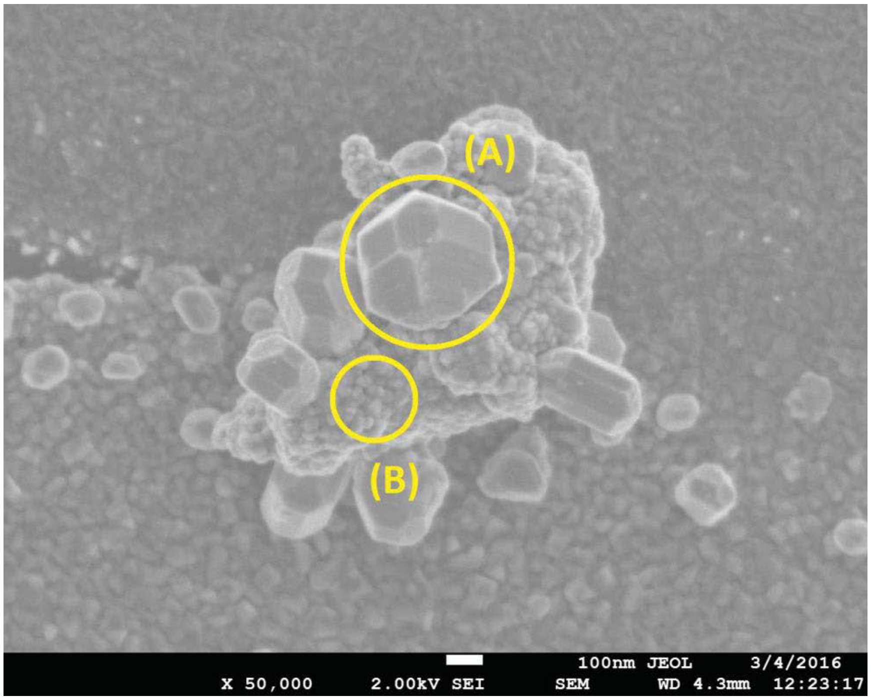

Figure 41 - Inner substrate large crystal growth

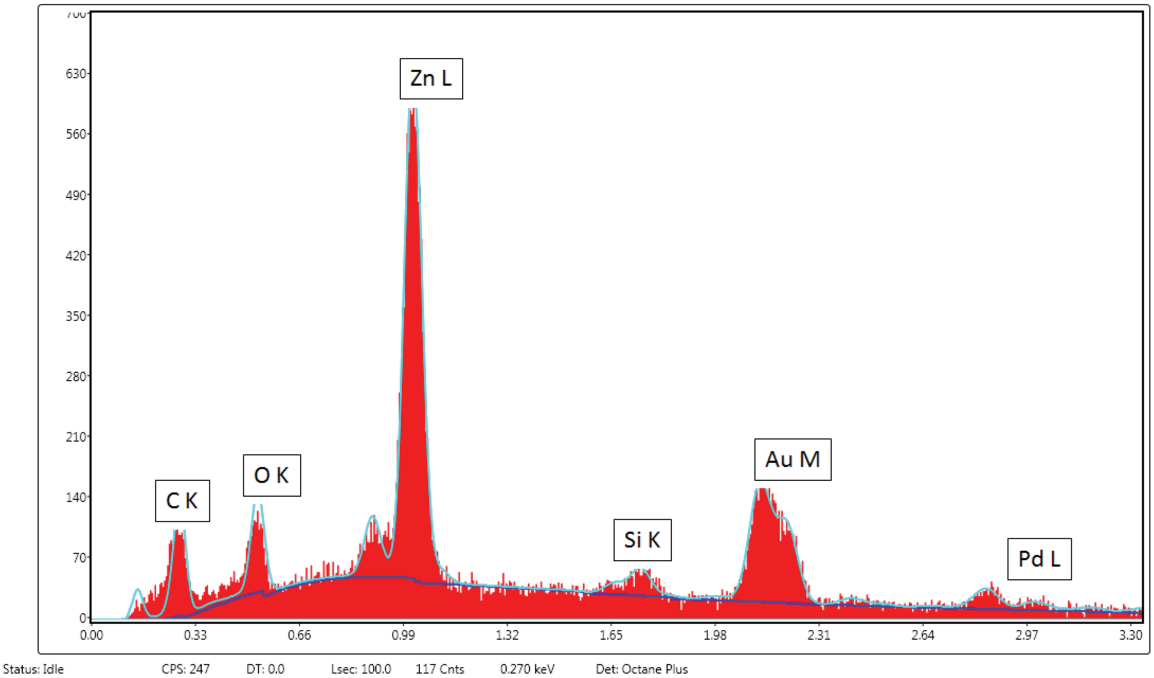

Status: Idle CPS: 247 DT: 0.0 Lsec: 100.0 117 Cnts 0.270 keV Det: Octane Plus

Figure 42 - EDS spectrum of large crystal (A in Figure 41) inner substrate growth

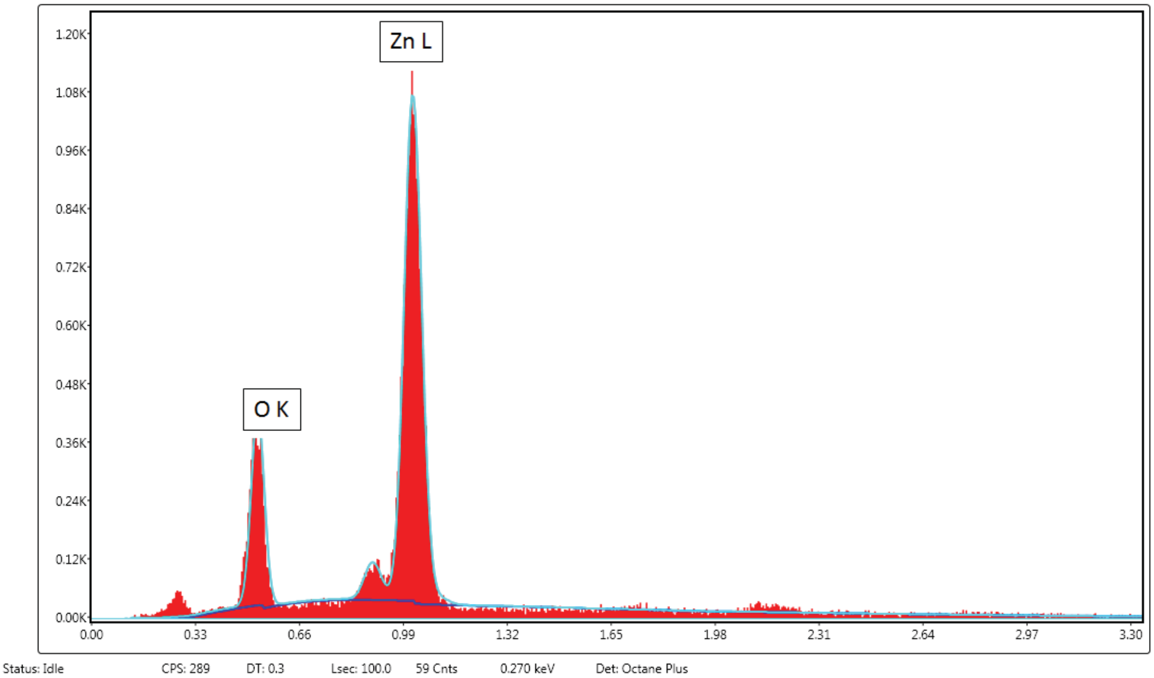

Status: Idle CPS: 289 DT: 0.3 Lsec: 100.0 59 Cnts 0.270 keV Det: Octane Plus

Figure 43 - EDS spectrum of surrounding material (B in Figure 41)

4.1.4 Thermocouple Deposition

In addition to substrate deposition, deposition of some kind was observed to occur on the thermocouple shielding upstream of the copper support. A micrograph of the deposition is shown in Figure 44. A sample of this material was scraped off of the thermocouples and examined in the SEM. A number of very fine nano-scale morphologies were observed, but according to the EDS spectrum gathered during analysis, the deposition consisted entirely of zinc. This implies that the deposition in this region occurred after the furnace had started but before the leak valve had been opened.

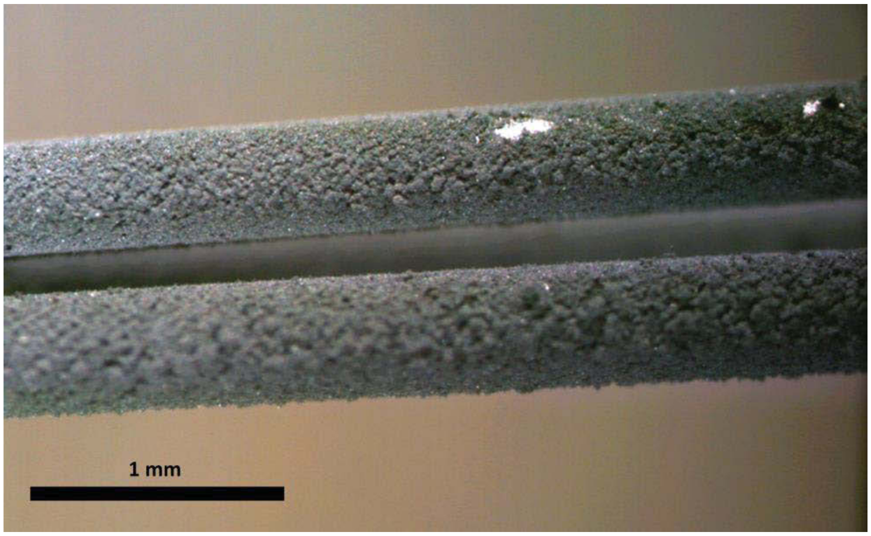

Figure 44 - Light microscopy image of deposition on thermocouple shielding.

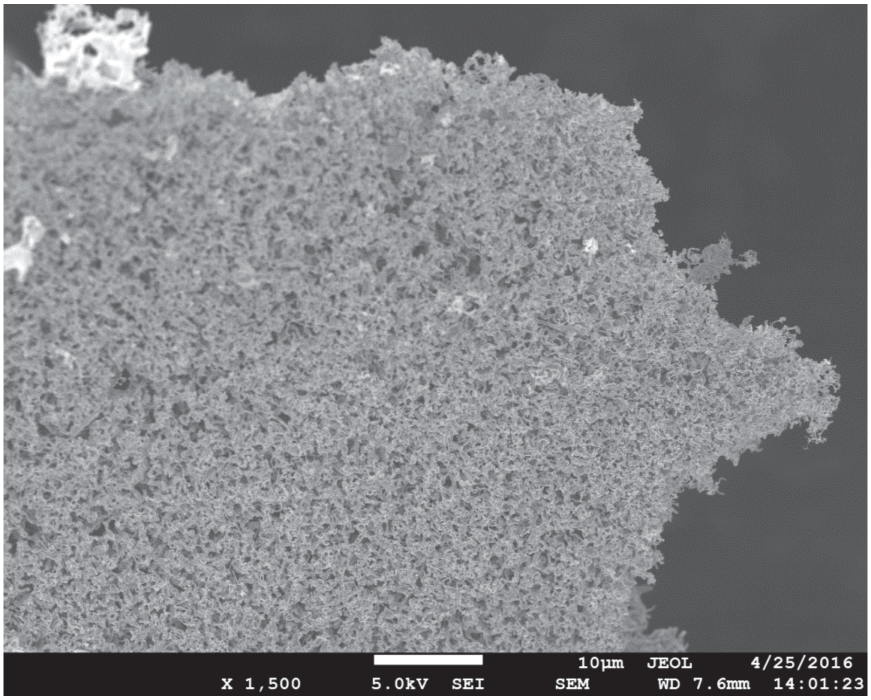

Figure 45 - Secondary electron image of thermocouple deposition

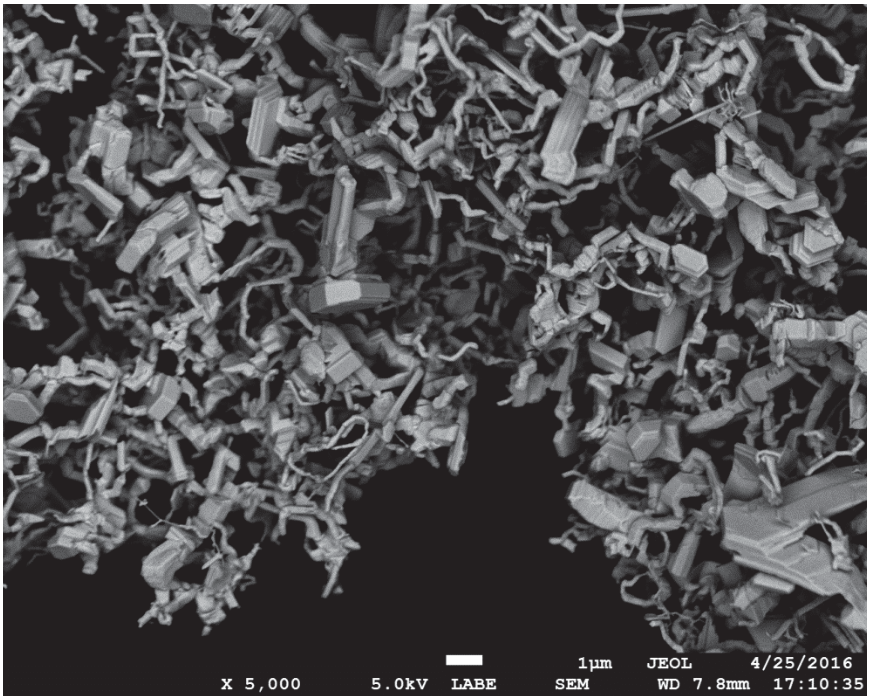

Figure 46 - Secondary electron image of thermocouple deposition, closer view

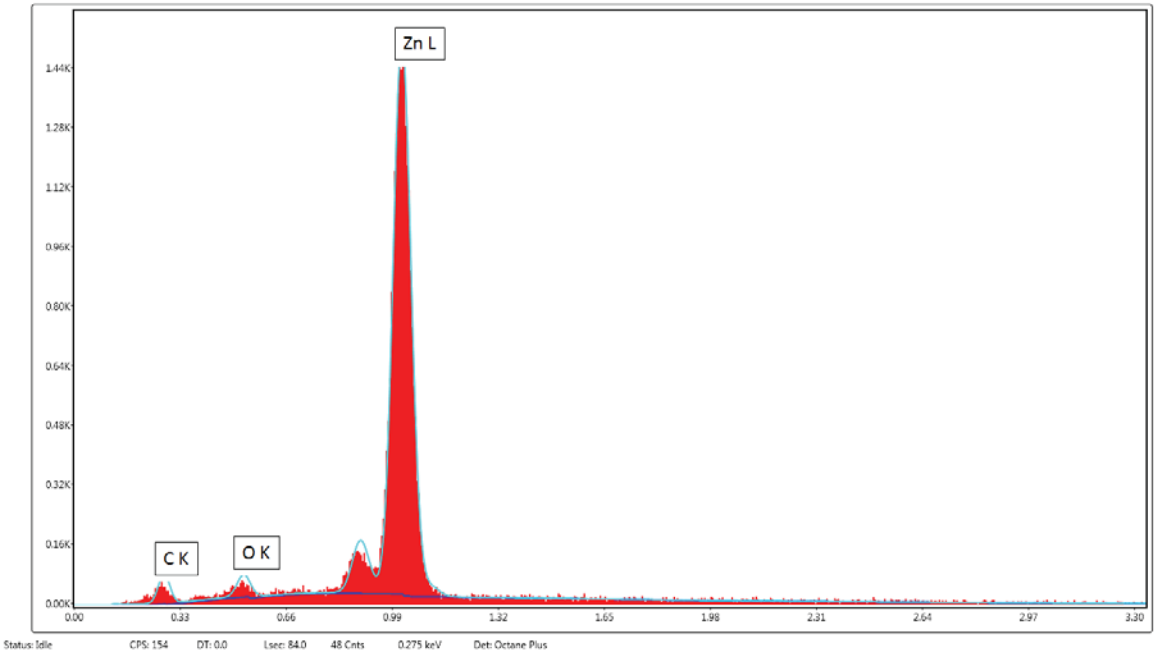

Figure 47 - EDS spectrum of thermocouple deposition

4.1.5 Remaining Zinc Powder

Some material left over from the experiment was found to remain on the copper support after the experiment had been completed. A low magnification image of some of the unevaporated metal powder can be seen in Figure 48, and a close view of the surface morphology can be seen in Figure 49. A backscattered electron image taken from the SEM (Figure 50) reveals a high compositional contrast in the morphology. Chemical analysis shows that the bright inclusions are primarily composed of zinc, while the rest of the surface morphology is zinc oxide.

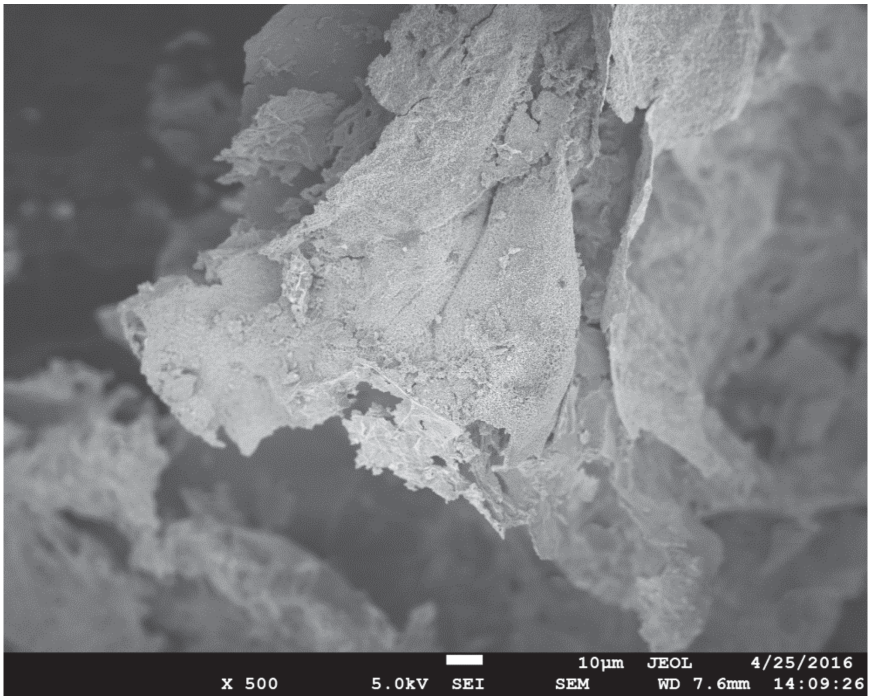

Figure 48 - Low magnification image of unevaporated metal powder

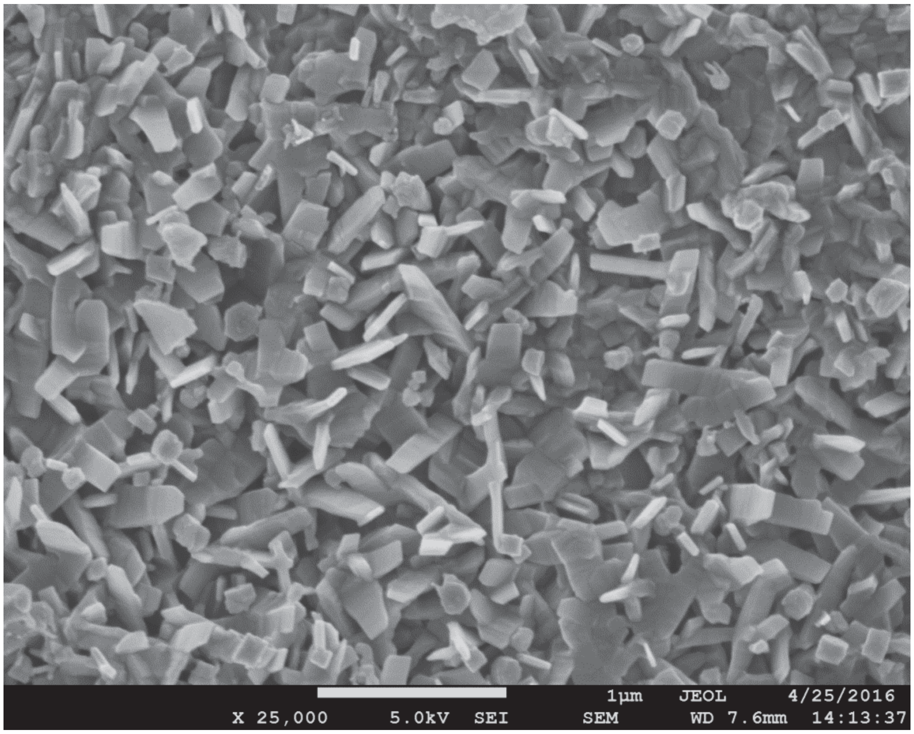

Figure 49 - Close view of unevaporated metal powder surface morphology

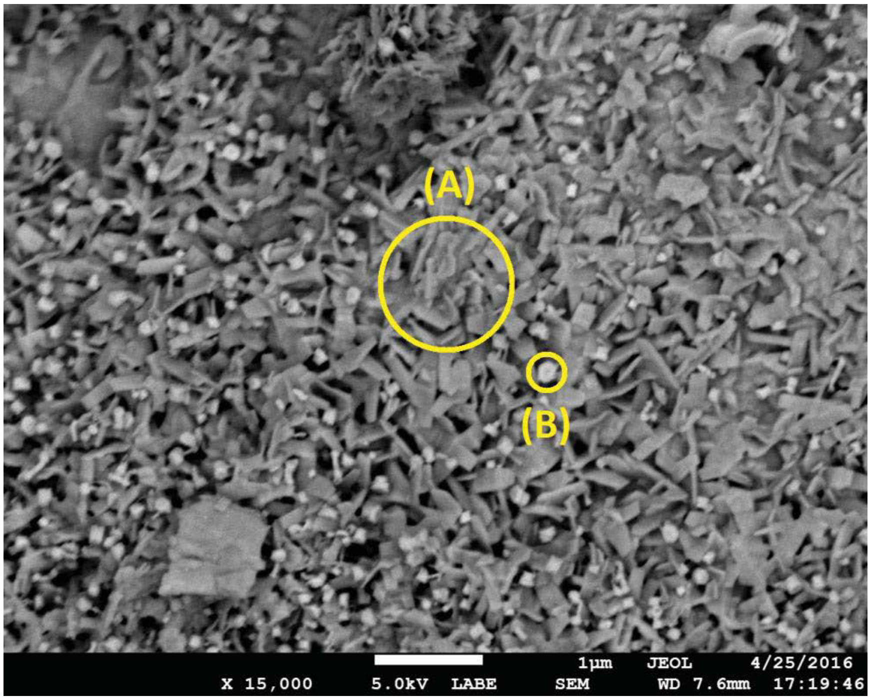

Figure 50 - Secondary electron image of unevaporated metal powder surface morphology

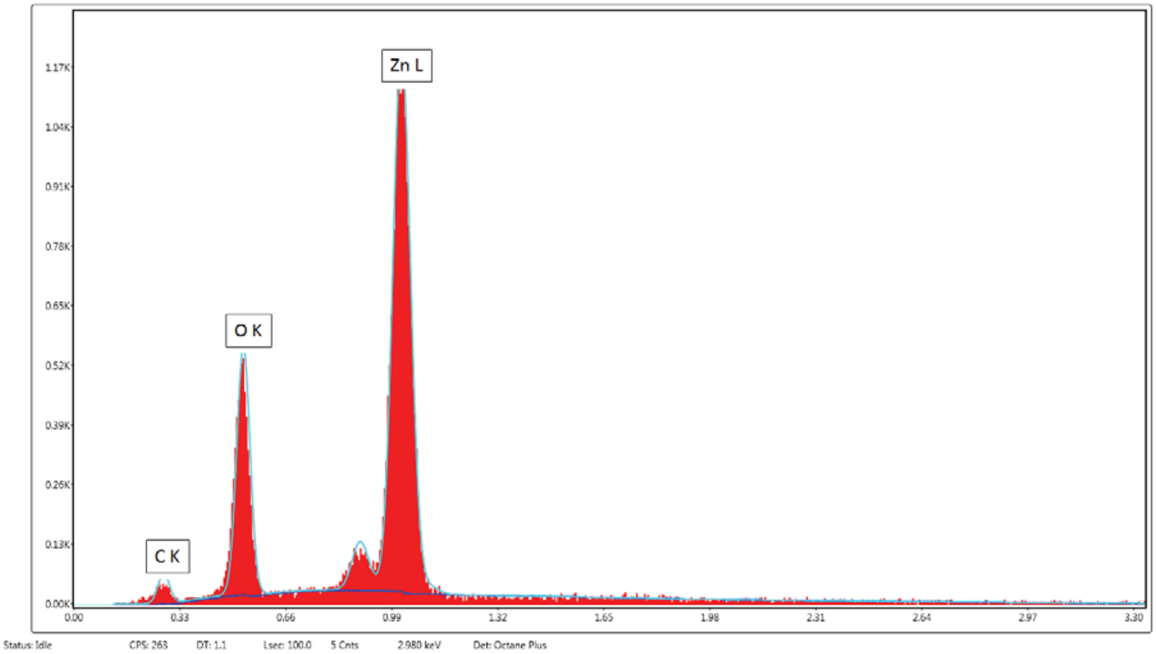

Figure 51 - EDS spectrum of dark region (A in Figure 50) on surface of unevaporated metal powder

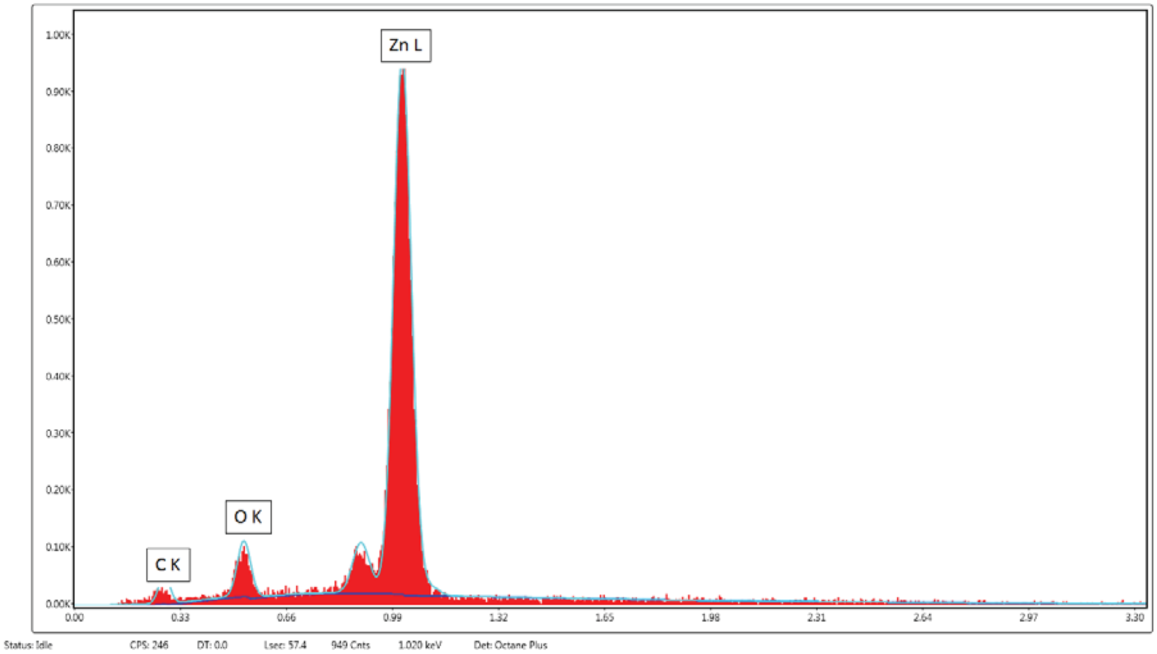

Figure 52 - EDS spectrum of light regions (B in Figure 50) on surface of unevaporated metal powder

4.2 CFD Model Verification

In order to verify the accuracy of the CFD model, model temperatures were compared to experimental measurements. The resulting data can be seen in Table 13, Figure 53, and Figure 54. Modeled temperatures followed a similar distribution to what was measured, but the difference between the modeled values and recorded values was large for both two- and three-dimensional models with an average difference of approximately 90 K between the predicted and measured results. This large difference in temperatures is due to the extremely low convection heat transfer that exists in low density flows and to the very high thermal conduction in the body of the thermocouple shielding, which is made of steel. The thermocouples ran along the bottom surface of the reactor to reach the region of interest and then pointed vertically upwards to different heights. As a result, the thermocouple shielding conducted the high temperature from the reactor surface to the tip of the thermocouple creating a false reading. At the same time, the convection in the flow was so small compared to the conduction in the thermocouple body that it was not able to bring the thermocouple tip to the flow temperature. Thus, a different method has to be employed in order to measure the fluid temperatures inside the furnace.

Table 13 - Model Verification Temperature Differences

	2D Model Temperature (K)	3D Model Temperature (K)	Experimental Temperature (K)	Difference from 2D model (K)	Difference from 3D model (K)
Thermocouple 1	714.22	712.43	804.98	90.76	92.55
Thermocouple 2	714.46	712.48	804.38	89.92	91.90
Thermocouple 3	714.27	712.37	805.27	91.01	92.91
Thermocouple 4	713.11	712.02	807.34	94.23	95.32

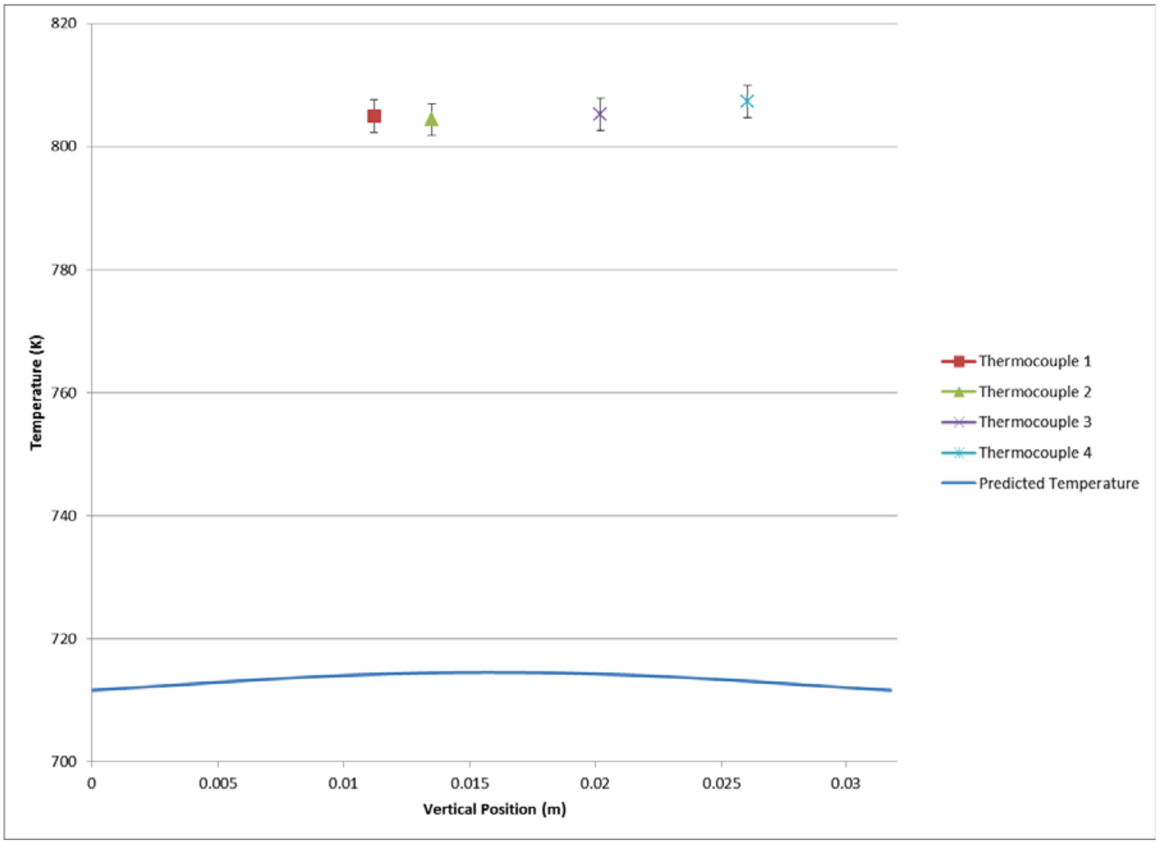

Figure 53 - Temperature vs Vertical Position for recorded temperatures and two-dimensional model between copper support and substrate

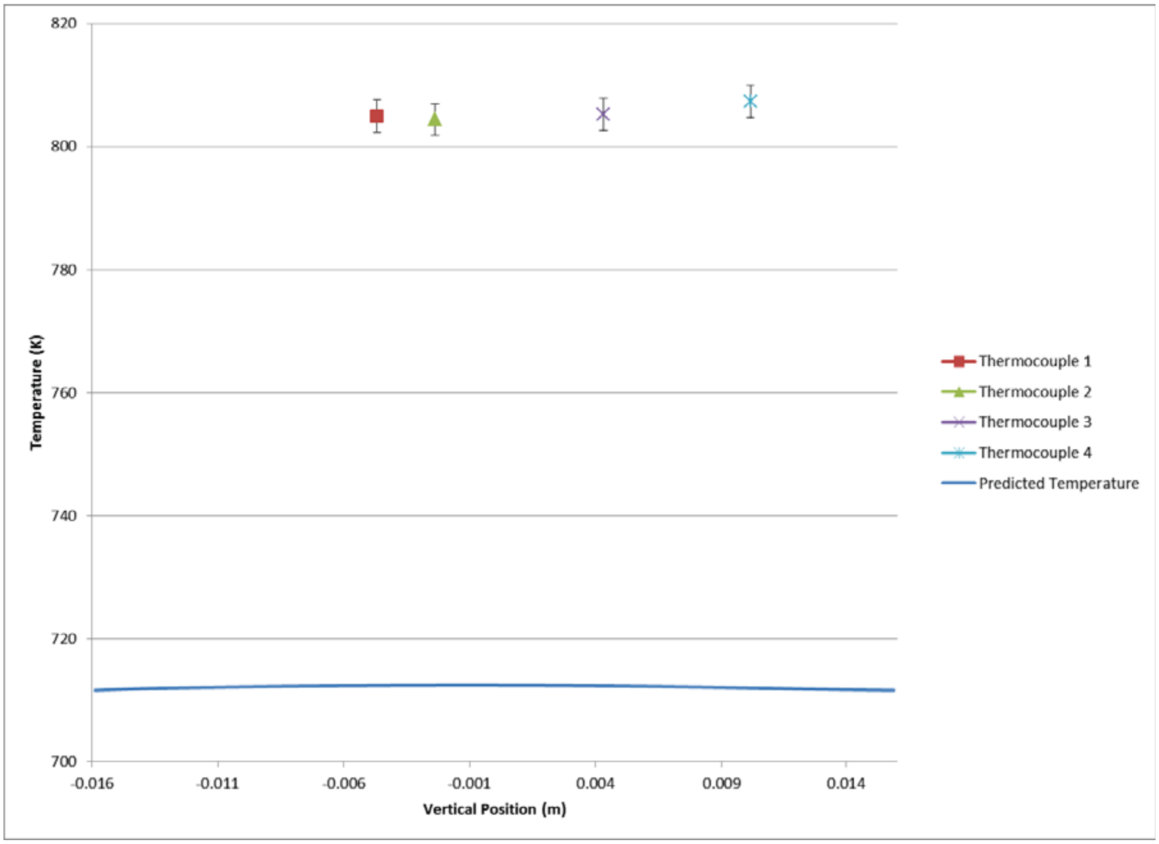

Figure 54 - Temperature vs Vertical Position for recorded temperatures and three-dimensional model between copper support and substrate

4.3 Modeling - Interior Conditions

The CFD portion of this work provided an estimate of the interior conditions during the reaction process, which proved to be of great importance, particularly since the measurement of fluid temperatures proved to be challenging. Comparisons were made between the two-dimensional and three-dimensional simulations, as well as between the two cases run. Each case was performed with a separate set of pressure boundary conditions corresponding to the proposed synthesis pressure conditions.

Velocities predicted by every model were quite high, with the lowest maximum velocity being 5.92 meters per second. This would normally result in a high Reynolds number, but the density of the fluid was extremely low due to the inlet and outlet boundary conditions. Maximum density in any model was 2.41e-4 kg/m^3. Because of this, Reynolds numbers were extremely low, as can be seen in Table 14.

Table 14 - Reynolds numbers predicted by models

	Reynolds number at point of highest velocity
13.33 Pa case – 2D model	1.001
13.33 Pa case – 3D model	0.528
6.67 Pa case – 2D model	0.523
6.67 Pa case – 3D model	0.297

As far as the agreement between two- and three-dimensional models is concerned, the contours of the results are quite close for the two-dimensional and three-dimensional CFD results, but there are large differences in magnitudes. Table 15 shows that the maximum values for temperature are identical for the two simulation types, but zinc mass fraction and velocity vary greatly.

Table 15 - Comparison of maximum values for 2D and 3D simulations

	13.33 Pa (100 mTorr)		6.67 Pa (50 mTorr)	
	2D	3D	2D	3D
Maximum Velocity (m/s)	24.2	10.6	12.6	5.92
Maximum Temperature (K)	805	805	805	805
Maximum Zinc Mass Fraction	0.191	0.848	0.317	0.847

Figure 59 through Figure 58 show plots of selected property values along the center of the furnace for each case run. Pressure values are quite close between the two simulation types (Figure 55 and Figure 56). The primary difference between the two pressure fields is the rate of pressure drop in the open regions on either side of the copper boat. Zinc mass percent can be seen to vary greatly between two- and three-dimensional models (Figure 57 and Figure 58). This is most likely cause by the differences in geometry. Two-dimensional simulation uses an assumed depth in order to compute flow rates and other values. For this simulation, the assumed depth was set to be the inner diameter of the tube (3.175 cm). As a result the cross-sectional area is functionally different between the two, which impacts the concentrations even when the flow rates are identical. This difference in concentrations leads to a change in mixture density (Figure 59 and Figure 60). The densities are quite close near the inlet of the furnace, but diverge as the difference in zinc concentrations increases.

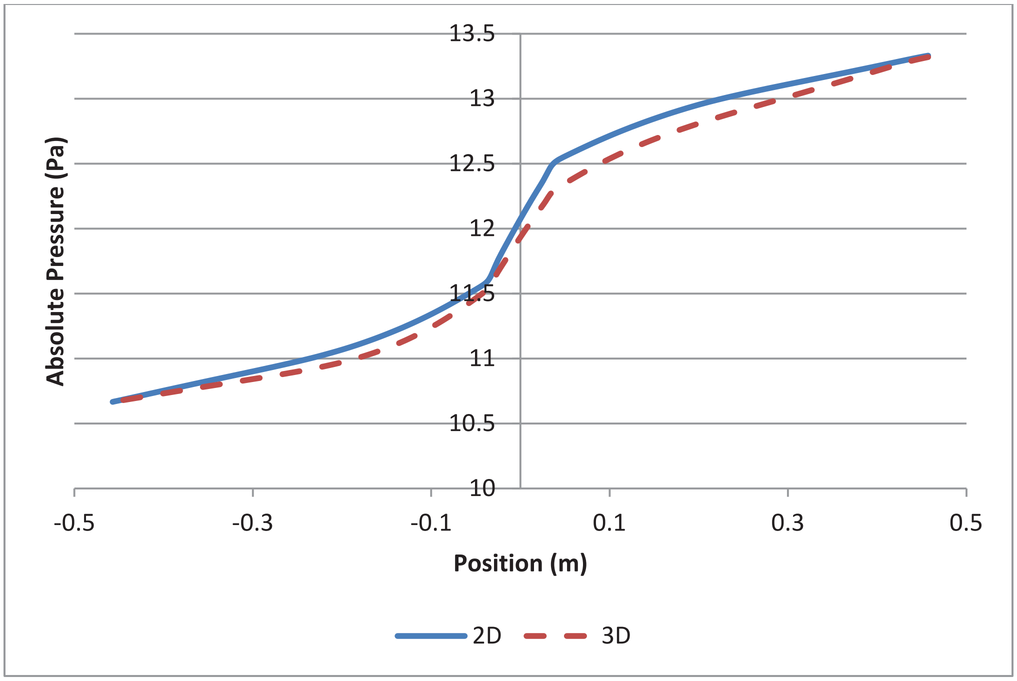

Figure 55 - Absolute pressure vs position for 13.33 Pa (100 mTorr)

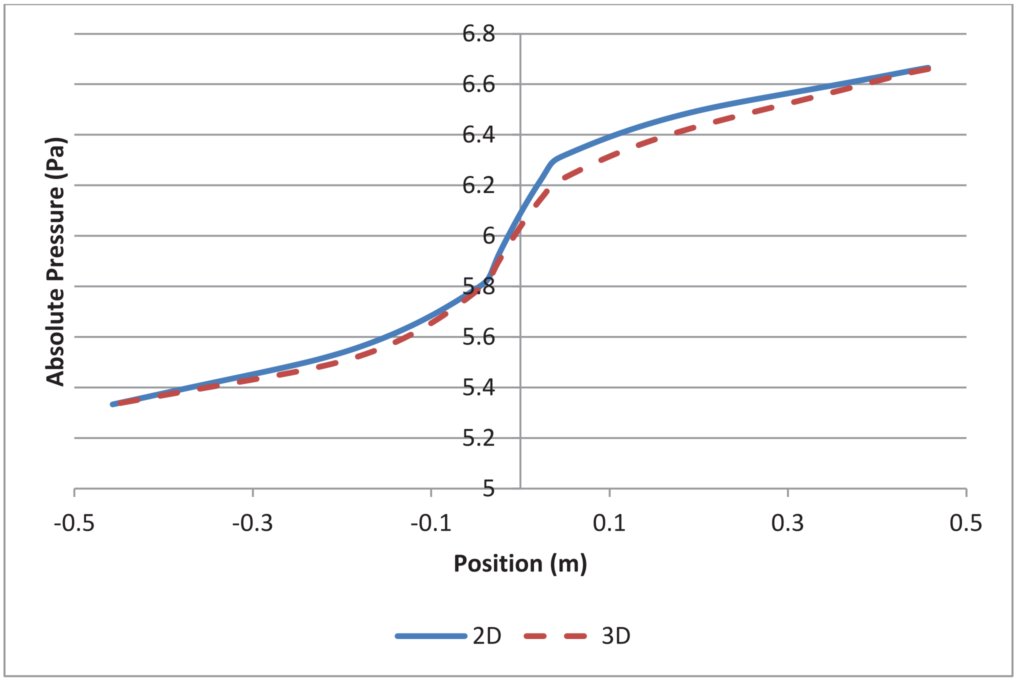

Figure 56 - Absolute pressure vs position for 6.67 Pa (50 mTorr) case

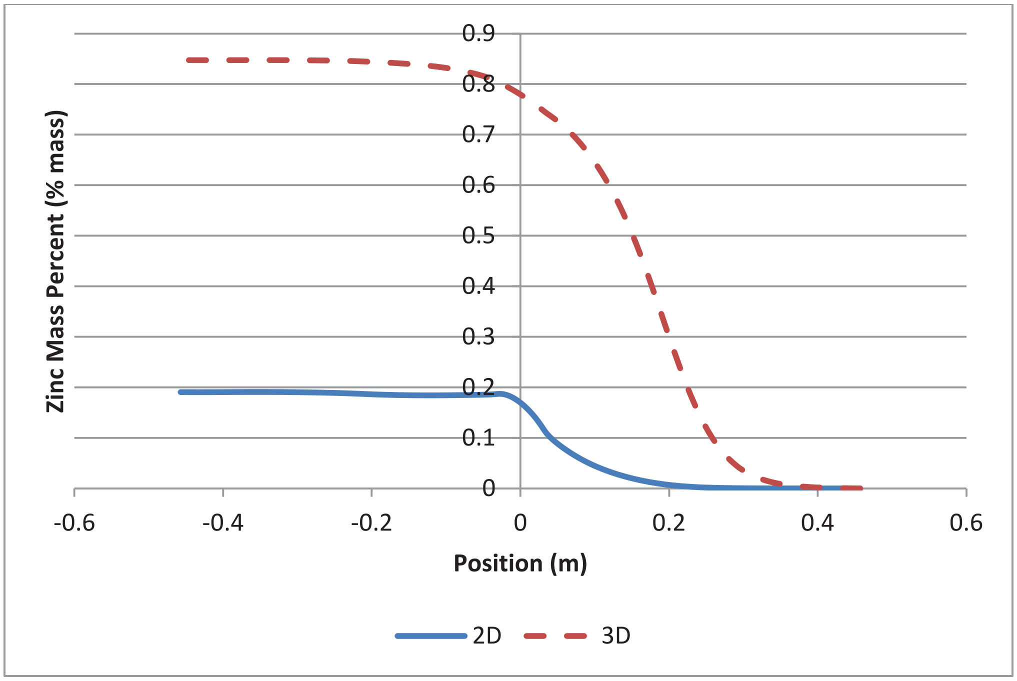

Figure 57 - Mass percent of zinc vapor vs position for 13.33 Pa (100 mTorr) case.

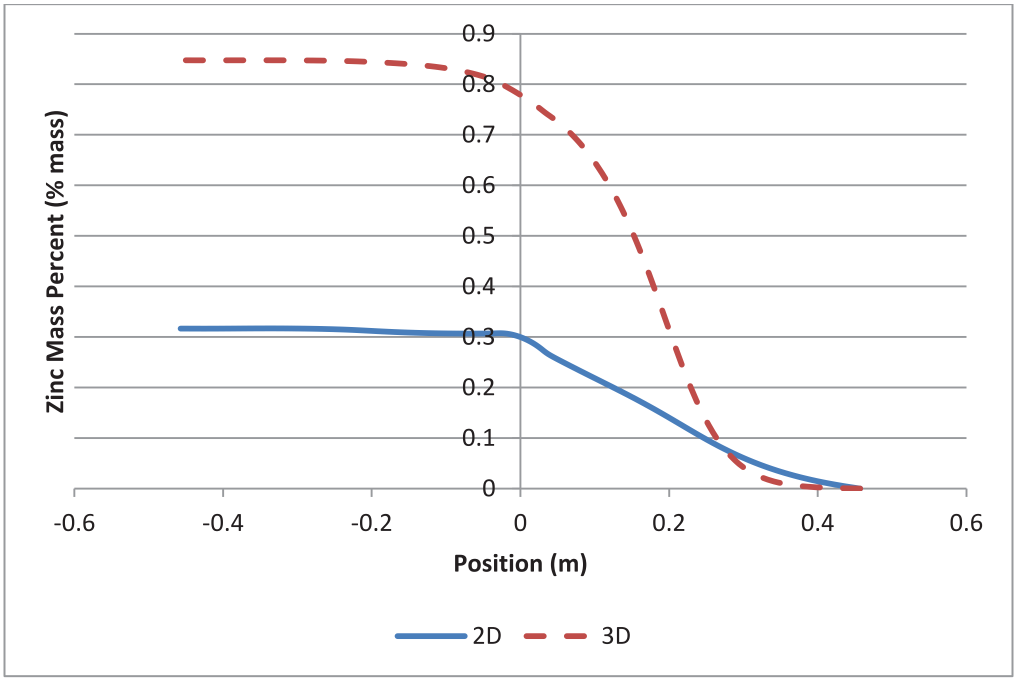

Figure 58 - Mass percent of zinc vapor vs position for 6.67 Pa (50 mTorr) case.

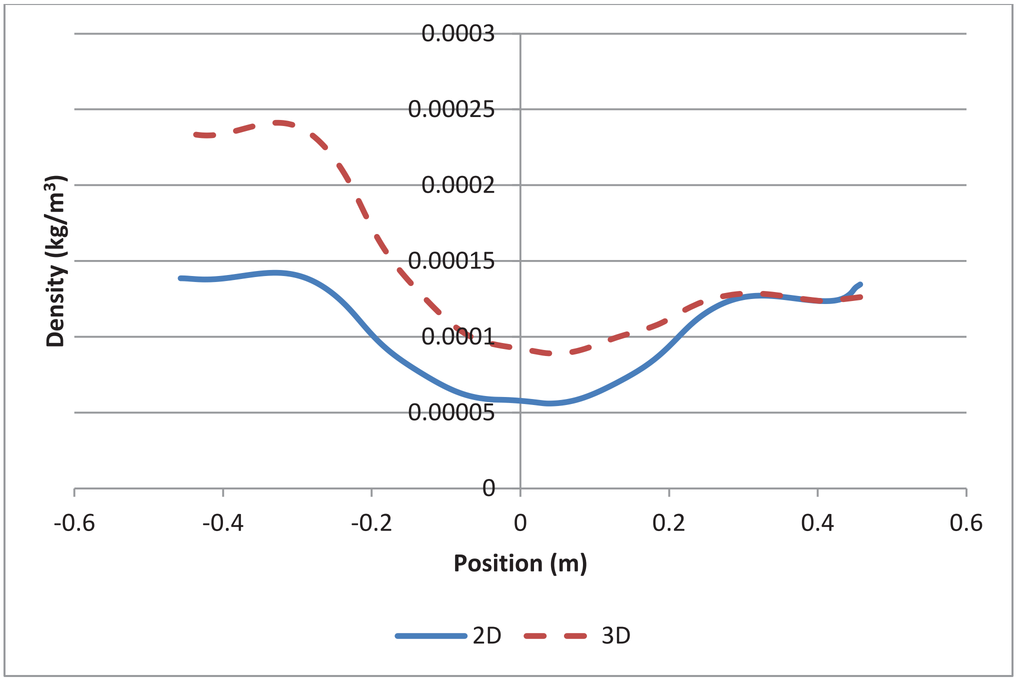

Figure 59 - Density vs position for 13.33 Pa (100 mTorr) case.

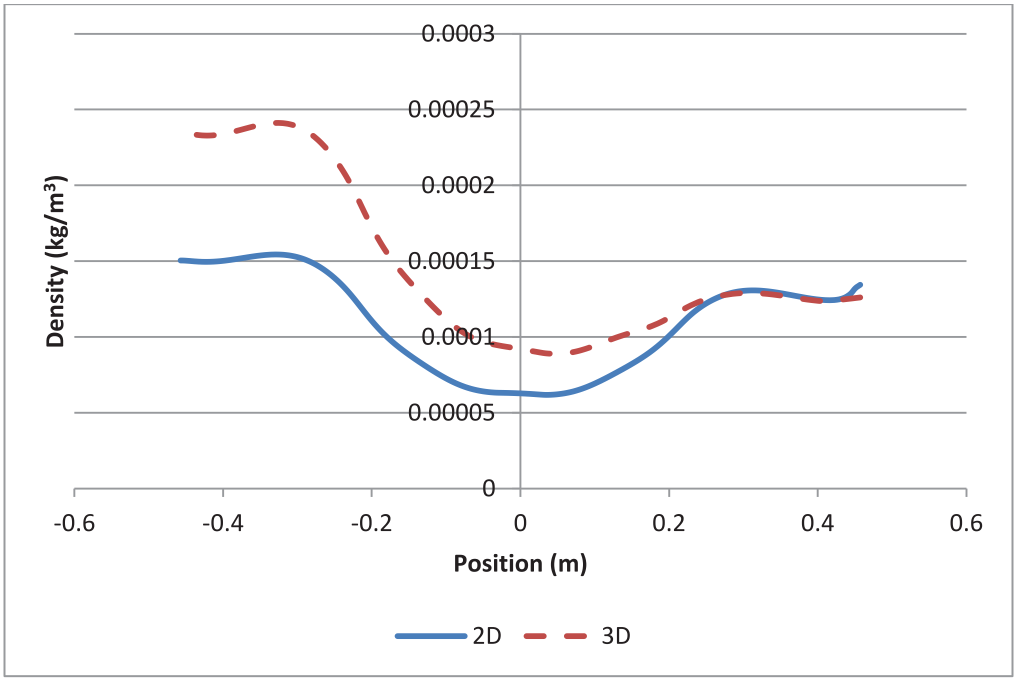

Figure 60 – Density vs position for 6.67 Pa (50 mTorr) case.

The simulations showed unexpected results in terms of temperature distribution. While the maximum velocities are quite high, the temperature distribution appears to be dominated by conduction rather than convection. Inspecting lines of equal temperature shows that convection does have an impact on temperature, but the effect is much smaller than would be normally expected (see Figure 61). The cause of this counter-intuitive temperature distribution is the extremely low densities and subsequently low Reynolds numbers of the fluid.

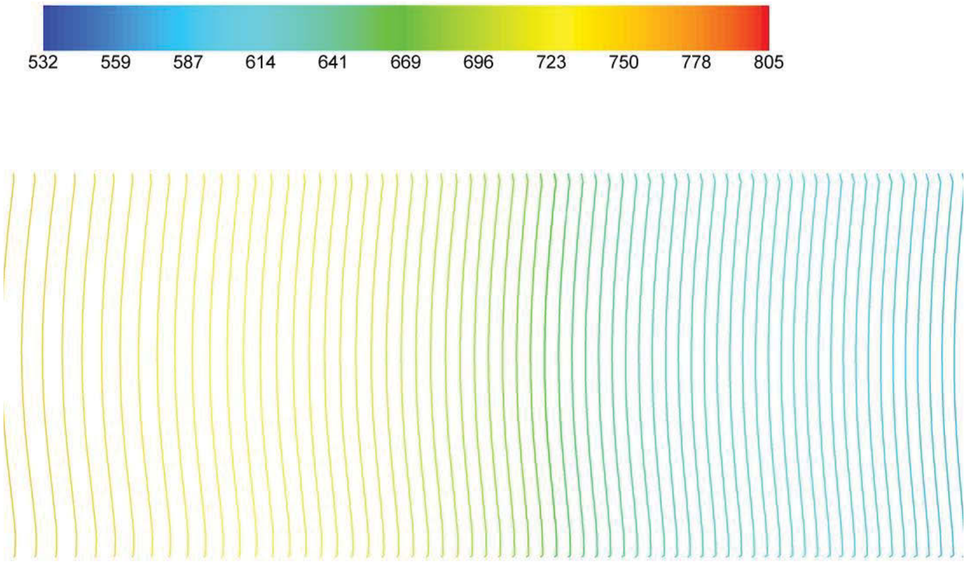

Figure 61 – Lines of equal temperature for 13.33 Pa case in three-dimensional model

In the following sections, four planes were used to examine cross-sections of the simulation results. Figure 62 indicates the location of each of these section planes as well as the label by which it will be identified. Plane (1) is located between the substrate and outlet, plane (2) is between the copper support and substrate, plane (3) is at the midpoint of the copper support, and plane (4) is between the inlet and copper support.

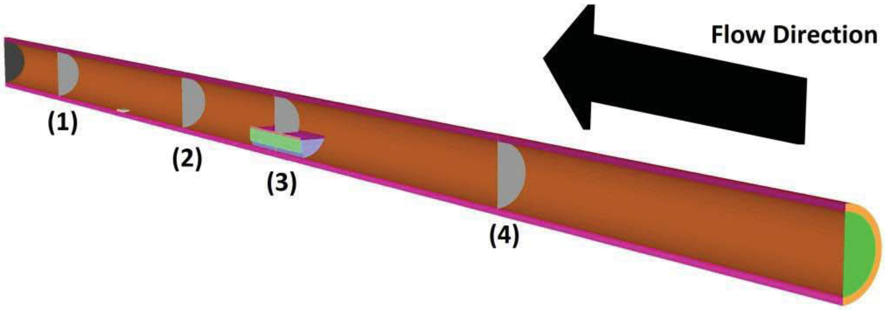

Figure 62 - Section planes for 3D model.

4.3.1 13.33 Pa (100 mTorr) Case

Contours of the results for the 13.33 Pa case can be seen in Figure 63 through Figure 67. Velocity contours are identical in shape but not magnitude, where the three-dimensional model has a maximum velocity of less than half of the two-dimensional model maximum velocity. Temperature profiles between the two are nearly identical. Zinc vapor mass fraction varied in both magnitude and contour, showing a large difference between the two models.

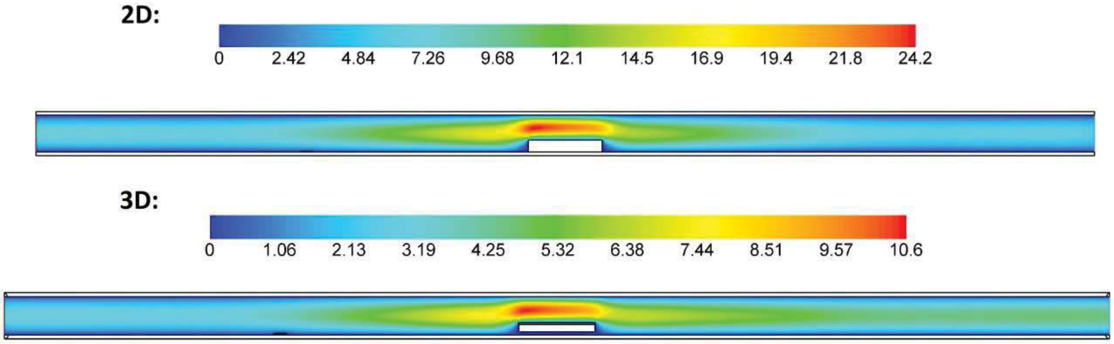

Figure 63 – Velocity (m/s) contour comparison for 13.33 Pa (100 mTorr) case.

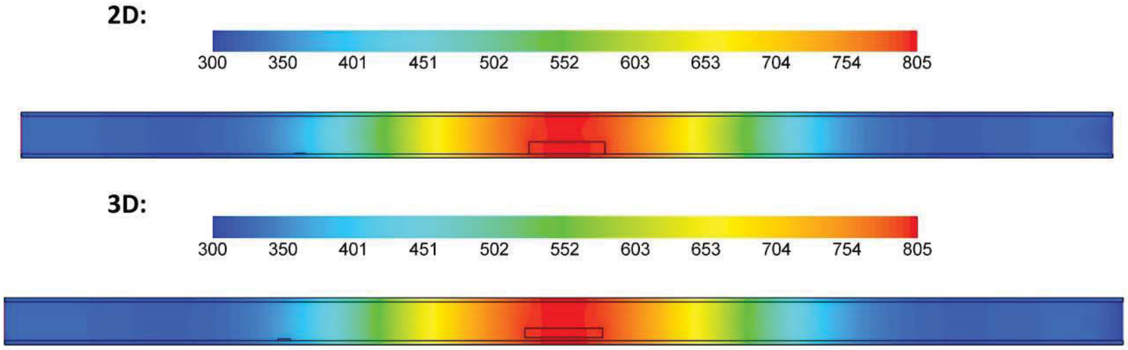

Figure 64 - Temperature (K) contour comparison for 13.33 Pa (100 mTorr) case.

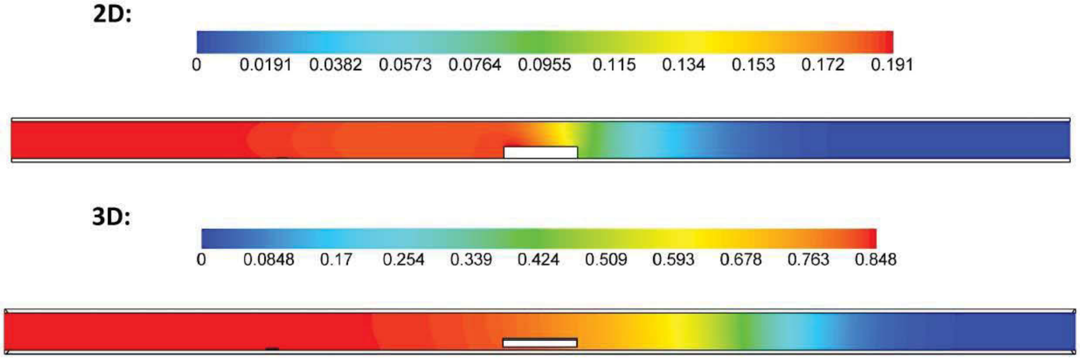

Figure 65 - Zinc mass fraction comparison for 13.33 Pa (100 mTorr) case.

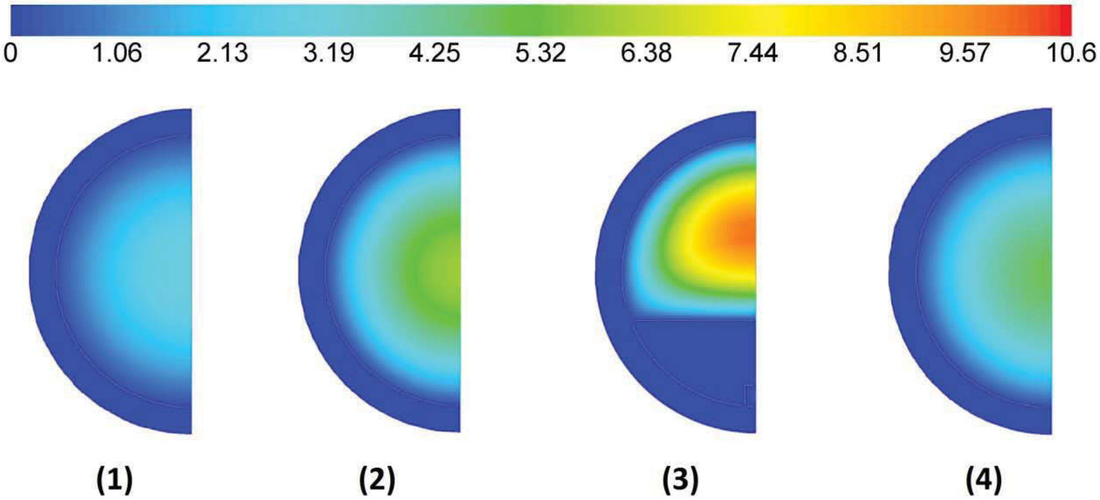

Figure 66 - Velocity sections for 13.33 Pa (100 mTorr) case.

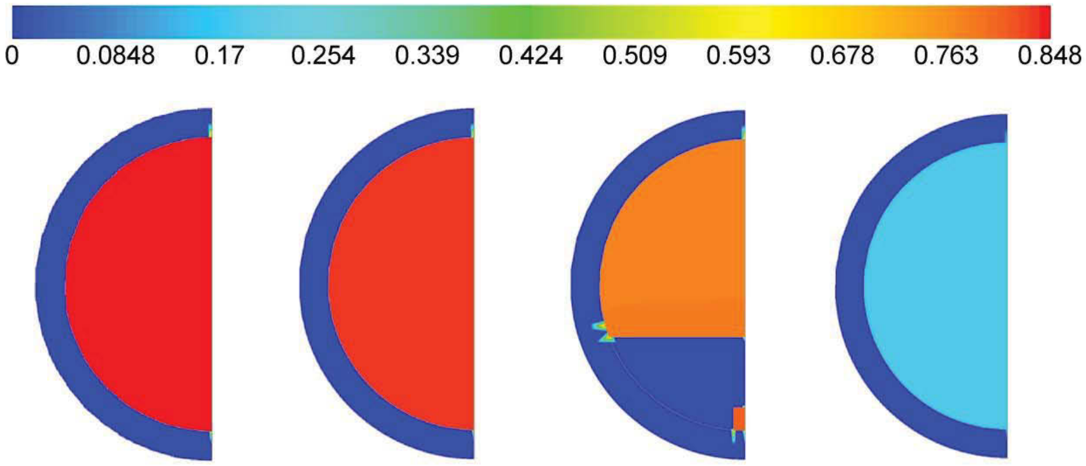

(1) (2) (3) (4)

Figure 67 - Zinc mass fraction sections for 13.33 Pa (100 mTorr) case.

The cross-sectional plots for velocity show a typical distribution for fully developed flow, while the zinc mass fraction cross sections show that the variation in mass fraction is minimal throughout a given section.

4.3.2 <u>6.67 Pa (50 mTorr) Case</u>

Contours of the results for the 6.67 Pa case can be seen in Figure 68 through Figure 72. Similarly to the 13.33 Pa case, the velocity contours of the two models are similar in shape, but greatly differing in magnitude, the temperature contours are nearly identical, and the zinc mass fraction contours are different in both shape and magnitude. Notably, the zinc mass fraction results are closer between the 2D and 3D models for this case.

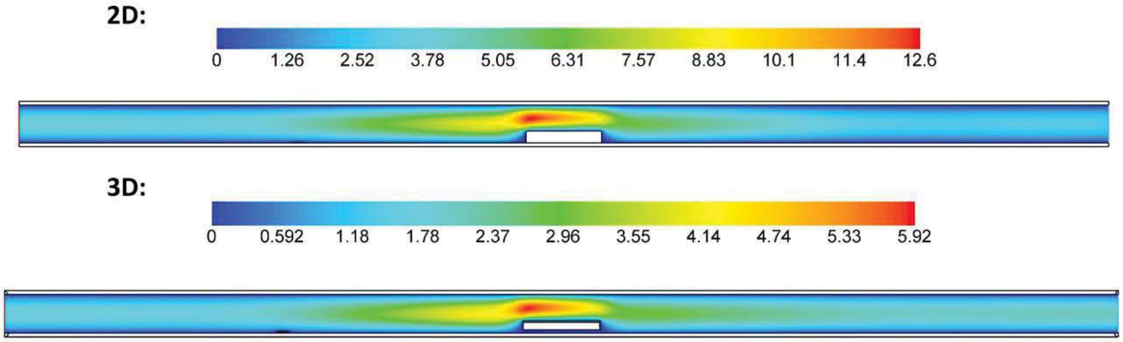

Figure 68 - Velocity comparison for 6.67 Pa (50 mTorr) case. Velocities in m/s

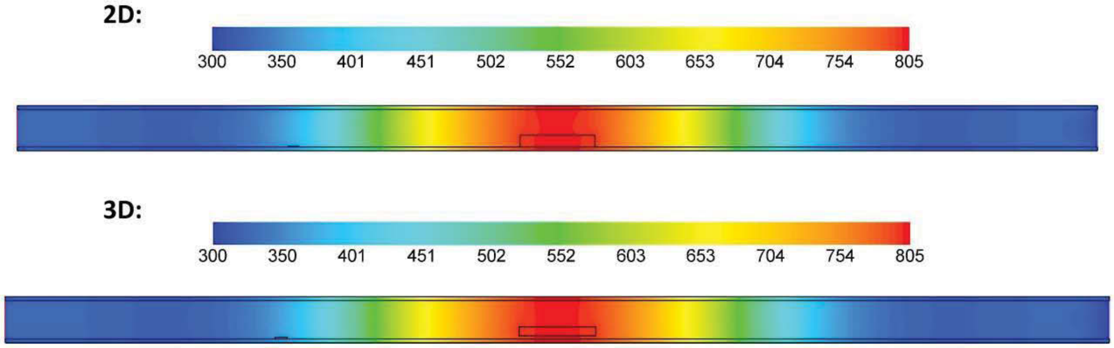

Figure 69 - Temperature comparison for 6.67 Pa (50 mTorr) case. Temperatures measured in K.

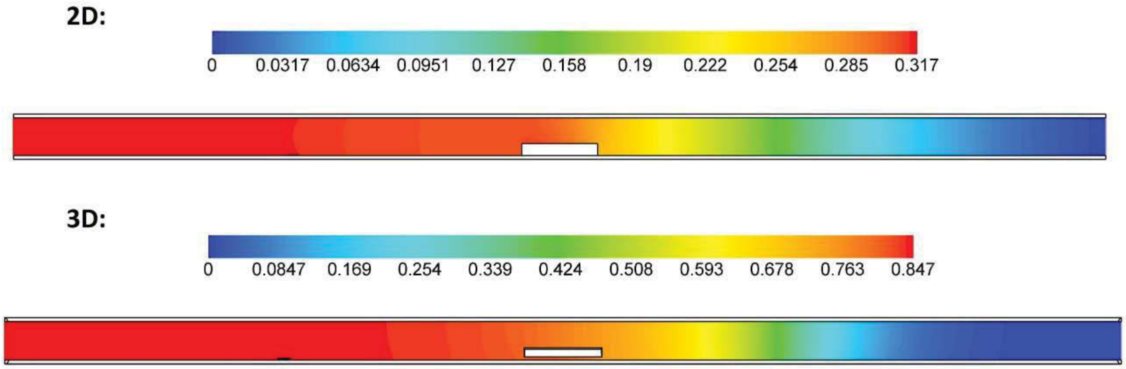

Figure 70 - Zinc mass fraction comparison for 6.67 Pa (50 mTorr) case.

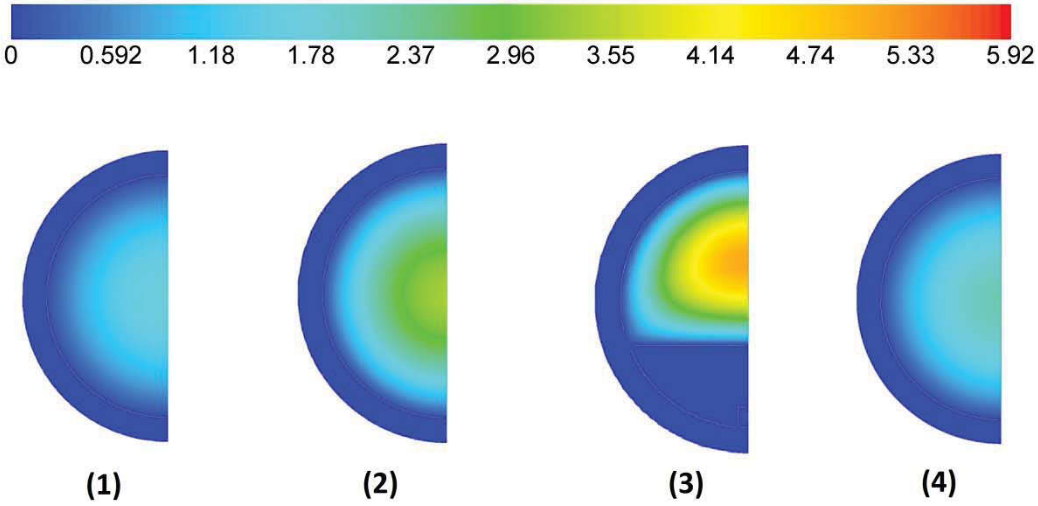

Figure 71 - Velocity sections for 6.67 Pa (50 mTorr) case.

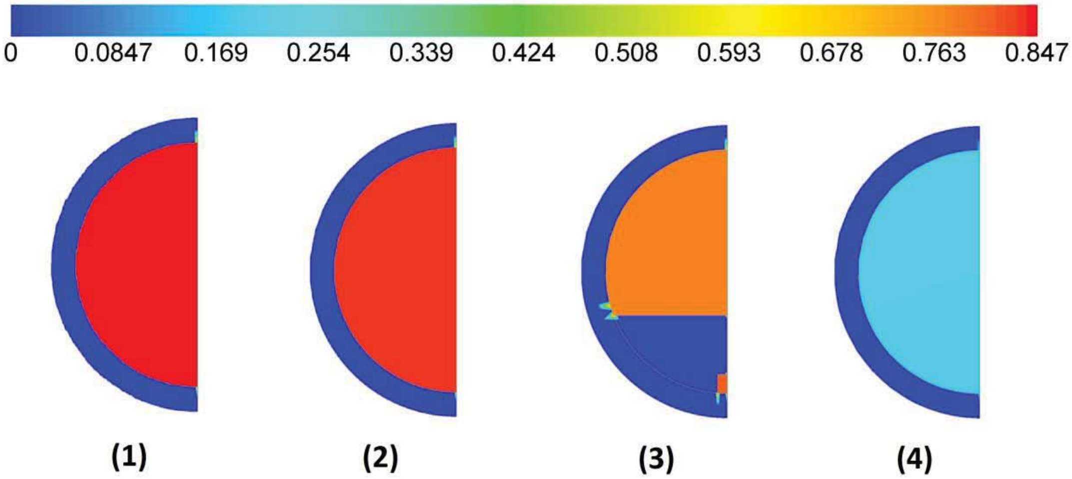

Figure 72 - Zinc mass fraction sections for 6.67 Pa (50 mTorr) case.

Again, note that even for a different set of boundary conditions, the cross-sectional plots for velocity show a typical distribution for fully developed flow, while the zinc mass fraction cross sections show little in terms of radial variation.

Chapter 5: Conclusions and Future Work

5.1 Conclusions

Zinc oxide nanostructures were successfully synthesized at several locations within the reactor, and predicted fluid properties were compared at each growth site, as can be seen in Table 16 and Table 17. The only property similar at each location was the zinc mass fraction, which was close in value at each location where zinc oxide was found to grow. Unfortunately, the experimental measurements need improvement in order to more accurately capture the reactor conditions so a full validation of the CFD models could be performed.

Table 16 - Properties at regions of zinc oxide growth from 2D model

	Density (kg/m^3)	Pressure (mTorr)	Temperature (K)	Velocity (m/sec)	Zinc Mass Fraction
Outer Substrate	6.86e-5	84.94	667	0.894	0.184
Inner Substrate	6.61e-5	85.19	690	0.927	0.185
Unevaporated Metal Powder	5.76e-5	90.57	804	2.167	0.163

Table 17 - Properties at regions of zinc oxide growth from 3D model

	Density (kg/m^3)	Pressure (mTorr)	Temperature (K)	Velocity (m/sec)	Zinc Mass Fraction
Outer Substrate	1.14e-4	84.17	667	1.015	0.834
Inner Substrate	1.10e-4	84.46	690	1.056	0.832
Unevaporated Metal Powder	9.21e-5	89.62	804	1.292	0.780

The model itself did serve as a useful tool for selecting possible substrate locations, particularly in terms of near-wall temperature. With further development and investigation, it is easy to imagine fluid modeling becoming a useful tool in optimization of CVD reactor design.

5.2 Future Work

There is much which can be improved about both the modeling and experimental portions of this work. The model itself is in need of much refinement. Verification of the model revealed a large discrepancy in recorded temperatures and predicted temperatures. Closer agreement between experiment and simulation must be achieved if any reliable correlations are to be developed. Additionally, the model could be modified to include surface chemistry, which could be used to more accurately model the deposition process. There is, however, some debate as to the actual mechanism of the reaction, and simulation of the reaction is not possible without knowing the required reaction coefficients, so using simulations to test varying theories of the reaction mechanism is another possible avenue of research.

Experimentally, reactor measurement instrumentation should be expanded and improved. Measurement of the temperature of the flow at the outlet of the reactor would help to verify the temperature gradient which the CFD models predict. A flow meter would provide an alternate boundary condition and verification tool for modeling considerations, and increasing the number of exterior thermocouples would increase the accuracy of the temperature polynomial used as a boundary condition.

Finally, parametric study of the reaction process, iterating on both the experiment and the simulation models should yield much insight into the effects that changing conditions have on the product nanostructures, which would ultimately allow for the development of mathematical correlations linking reactor parameters to product yield, allowing for optimization of a zinc oxide nanostructure production process.

References

[1] H. Kind, H. Yan, B. Messer, M. Law and P. Yang, "Nanowire Ultraviolet Photodetectors and Optical Switches," *Advanced Materials,* vol. 14, no. 2, pp. 158-160, Jan 2002.

[2] W. I. Park, J. S. Kim, G.-C. Yi, M. H. Bae and H.-J. Lee, "Fabrication and electrical characteristics of high-performance ZnO nanorod field-effect transistors," *Applied Physics Letters,* vol. 85, no. 21, pp. 5052-5054, 22 Nov 2004.

[3] Z. L. Wang and J. Song, "Piezoelectric Nanogenerators Based on Zinc Oxide Nanowire Arrays," *Science,* vol. 312, no. 5771, pp. 242-246, 2006.

[4] J. L. Gomez and O. Tigli, "Zinc oxide nanostructures: from growth to application," *Journal of Materials Science,* vol. 48, pp. 612-624, 2013.

[5] K.-K. Kim, J.-H. Song, H.-J. Jung, W.-K. Choi, S.-J. Park and J.-H. Song, "The grain size effects on the photoluminescence of ZnO/α-Al2O3 grown by radio-frequency magnetron sputtering," *Journal of Applied Physics,* vol. 87, no. 7, pp. 3573-3575, 1 Apr 2000.

[6] T. N. Oder, A. Smith, M. Freeman, M. Mcmaster, B. Cai and M. L. Nakarmi, "Properties of ZnO Thin Films Codoped with Lithium and Phosphorus.," *Journal of Electronic Materials,* vol. 43, no. 5, pp. 1370-1378, May 2014.

[7] Z. Chen, K. Shum, T. Salagaj, W. Zhang and K. Strobl, "ZnO thin films synthesized by chemical vapor deposition," in *Applications & Technology Conference (LISAT)*, 2010.

[8] T. Hsueh, S. Chang, C. Hsu, Y. Lin and I. Chen, "Highly sensitive ZnO nanowire ethanol sensor with Pd adsorption," *Applied Physics Letters,* vol. 91, 2007.

[9] X. Wang, L. Qingwen, L. Zhibo, J. Zhang, Z. Liu and R. Wang, "Low-temperature growth and properties of ZnO nanowires," *Applied Physics Letters,* vol. 84, pp. 4941-4943, 2004.

[10] J. T. Black and R. A. Kohser, DeGarmo's Materials and Processes in Manufacturing, 11th ed., Hoboken, NJ: John Wiley & Sons, 2012, p. 1069.

[11] H. Tian, J. Xu, Y. Tian, P. Deng and H. Wen, "Effect of different O2/N2 flow rate on the size and yield of ZnO nanostructures," *CrystEngComm,* no. 13, pp. 2544-2548, 2013.

[12] T. M. Trad, K. B. Donley, D. C. Look, K. G. Eyink, D. H. Tomich and C. R. Taylor, "Low temperature deposition of zinc oxide nanoparticles via zinc-rich vapor phase transport and condensation.," *Journal of Crystal Growth,* vol. 312, no. 24, pp. 3675-3679, Jun 2010.

[13] G. Shen, Y. Bando and C.-J. Lee, "Synthesis and Evolution of Novel Hollow ZnO Urchins by a Simple Thermal Evaporation," *Journal of Physical Chemistry B,* vol. 109, no. 21, pp. 10578-10583, 2 Jun 2005.

[14] D.-S. Kang, S. K. Han, S. M. Yang, J. G. Kim, W. J. Hwang, S.-K. Hong and J. W. Lee, "Growth and Characterization of Zinc Oxide Nanostructures on," *Journal of the Korean Physical Society,* vol. 53, no. 1, pp. 292-298, July 2008.

[15] H. Tian, J. Xu, Y. Tian, P. Deng and H. Wen, "Morphological evolution of ZnO nanostructures: experimental and preliminary simulation studies," *CrystEngComm,* no. 17, 2012.

[16] B. K. Ozcelik and C. Ergun, "Synthesis of ZnO nanoparticles by an aerosol process," *Ceramics International,* vol. 40, no. 5, pp. 7107-7116, 2014.

[17] Y. Çengel and M. Boles, Thermodynamics: An Engineering Approach, McGraw-Hill, 2008.

[18] K. Kadoya, N. Matsunaga and A. Nagashima, "Viscosity and Thermal Conductivity of Dry Air in the Gaseous Phase," *Journal of Physical Chemistry,* vol. 14, no. 4, pp. 947-970, 1985.

[19] R. Bird, W. Steward and E. Lightfoot, Transport Phenomena, New York: Wiley, 1960.

[20] R. Tena-Zaera, M. Martínez-Tomás, S. Hassani, R. Triboulet and V. Muñoz-Sanjosé, "Study of the ZnO crystal growth by vapour transport methods," *Journal of Crystal Growth,* vol. 270, pp. 711-721, 2004.